Paull, C.K., Matsumoto, R., Wallace, P.J., et al., 1996
Proceedings of the Ocean Drilling Program, Initial Reports, Vol. 164

5. SITES 991/992/993[1]

Shipboard Scientific Party[2]

HOLE 991A

Position: 32°59.018′N, 75°55.801′W

Start hole: 0030 hr, 5 November 1995

End hole: 1415 hr, 5 November 1995

Time on hole: 13.75 hr (0.57 days)

Seafloor (drill pipe measurement from rig floor, mbrf): 2578.4

Total depth (drill pipe measurement from rig floor, mbrf): 2635.0

Distance between rig floor and sea level (m): 10.9

Water depth (drill pipe measurement from sea level, m): 2567.5

Penetration (mbsf): 56.6

Coring totals:
Type: APC
Number: 6
Cored: 56.6 m
Recovered: 58.7 m (103.6%)

Formation:
Unit I: 0–2.05 mbsf; late Pleistocene; gray nannofossil clay and nannofossil silty clay
Unit II: 2.05–47.66 mbsf; late Pleistocene to late Miocene; deformed clay conglomerates of gray nannofossil silty clay
Unit III: 47.66–57.16 mbsf; late Miocene; dark olive gray nannofossil-rich clay, nannofossil-bearing clay in lower part

HOLE 991B

Position: 32°59.018′N, 75°55.796′W

Start hole: 1415 hr, 5 November 1995

End hole: 2000 hr, 5 November 1995

Time on hole: 5.75 hr (0.24 days)

Seafloor (drill pipe measurement from rig floor, mbrf): 2578.4

Total depth (drill pipe measurement from rig floor, mbrf): 2629.4

Distance between rig floor and sea level (m): 10.9

Water depth (drill pipe measurement from sea level, m): 2567.5

Penetration (mbsf): 51.0

Coring totals:
Type: PCS
Number: 2
Cored: 2.0 m
Recovered: 1.0 m (52.0%)

Formation:
Core recovered only from a limited interval (see "Operations" section, this chapter). Lithology is similar to Hole 991A.

HOLE 992A

Position: 32°58.542′N, 75°54.961′W

Start hole: 2330 hr, 5 November 1995

End hole: 0645 hr, 6 November 1995

Time on hole: 7.25 hr (0.30 days)

Seafloor (drill pipe measurement from rig floor, mbrf): 2597.7

Total depth (drill pipe measurement from rig floor, mbrf): 2648.0

Distance between rig floor and sea level (m): 10.9

Water depth (drill pipe measurement from sea level, m): 2586.9

Penetration (mbsf): 50.3

Coring totals:
Type: APC
Number: 6
Cored: 50.3 m
Recovered: 52.62 m (104.6%)

Formation:
Unit I: 0–9.1 mbsf; Pleistocene; deformed clay conglomerates of gray nannofossil silty clay
Unit II: 9.1–50.75 mbsf; late Miocene; dark greenish gray diatom-rich nannofossil clay

HOLE 993A

Position: 32°57.779′N, 75°53.685′W

Start hole: 0845 hr, 6 November 1995

End hole: 0615 hr, 7 November 1995

Time on hole: 21.50 hr (0.90 days)

Seafloor (drill pipe measurement from rig floor, mbrf): 2652.6

Total depth (drill pipe measurement from rig floor, mbrf): 2704.5

Distance between rig floor and sea level (m): 10.9

Water depth (drill pipe measurement from sea level, m): 2641.8

Penetration (mbsf): 51.9

Coring totals:
Type: APC
Number: 1
Cored: 1.9 m
Recovered: 1.88 m (98.9%)

Type: XCB
Number: 5
Cored: 50.0 m
Recovered: 43.8 m (87.6%)

---

[1] Paull, C.K., Matsumoto, R., Wallace, P.J., et al., 1996. *Proc. ODP, Init. Repts.,* 164: College Station, TX (Ocean Drilling Program).

[2] Shipboard Scientific Party is given in the list of participants that precedes the Table of Contents.

Formation:

Unit I: 0–47.27 mbsf; late Miocene; dark greenish gray nannofossil clay

Principal results: Sites 991, 992, and 993 form a transect across the crest of the Cape Fear Diapir, which breeches the seafloor within the scar of the giant Cape Fear Slide. Although this diapir occurs within a region where bottom-simulating reflectors (BSRs) are common, the continuity of the BSR is lost on the flanks of the diapir. Short (~50 m) holes were drilled at each of the three sites to investigate the effects of diapir intrusion and large-scale sediment failure on the regional gas hydrate field and on the transport of fluid and gas through the sedimentary sequence. A second major objective was to establish the nature of the core material of the diapir.

Site 991 is located on the upslope flank of the diapir where sediments that are deformed by diapir emplacement, but not actually part of the diapir's core, could be sampled. Lithologic variations, physical properties changes, and the nannofossil biostratigraphy indicate that a discontinuous Neogene sediment section was recovered at Hole 991A. The uppermost unit (Unit I, 0–2.05 mbsf) consists of gray nannofossil silty clay with a sharp, irregular contact at its base. Unit II (2.05–47.66 mbsf) is composed of firmer gray nannofossil silty clays. The top (2.05–12.67 mbsf) and bottom (18.37–47.66 mbsf) of this unit are characterized by zones of steeply dipping, discordant, and/or truncated beds of variegated colors; beds deformed by flowage, folding, and faulting; and mud clasts of various sizes, shapes, and colors. Although the middle (18.37–47.66 mbsf) of this unit appears undeformed, nannofossils indicate that an age reversal occurs at 18.37 mbsf and that this section between 18.37 and about 26 mbsf is a repeat section. Unit II is thus interpreted as a large slide block. A significant unconformity, correlative with earliest Pleistocene to early late Pliocene times, was detected within Unit II at ~26 mbsf. However, this unconformity was not associated with a lithologic change. Unit III (47.66–57.16 mbsf) is predominantly undeformed dark gray nannofossil-rich clay. The age of sediment recovered from the bottom of the hole is late Miocene (CN9b Subzone).

Site 992 is located near the topographic crest of the Cape Fear Diapir. Drilling in Hole 992A revealed two major lithologic units. The top unit (Unit I, 0–9.1 mbsf) is composed of strongly deformed gray nannofossil silty clay beds, which are similar in lithology and structural style to Unit II in Hole 991A. The unit appears to represent a mass-transport deposit that was emplaced by slumping. The bottom unit (Unit II, 9.1–50.75 mbsf) is a homogeneous olive gray diatom-rich nannofossil clay that appears to be undeformed. At Hole 992A, the uppermost Quaternary and the entire Pliocene to middle upper Miocene sequences are missing. The oldest sediment recovered was middle late Miocene in age (CN9a Subzone). The major lithologies did not reveal the composition of the underlying diapir.

Site 993 is situated on the southern flanks of the diapir in an area where previous sonar, photography, and coring indicated that jointed, allochthonous materials of diverse Neogene ages are exposed on the seafloor (Paull et al., 1989). Only one major unit was delineated in Hole 993A: Unit I (0–47.27 mbsf), which consists predominantly of gray nannofossil clay. The material is generally homogeneous greenish to olive gray nannofossil clay and silty clay. The only exception is a short interval from 4.43 to 4.9 mbsf that contains an indurated carbonate nodule and overlies a carbonate silty clay. Apart from the top 6 cm, the entire sequence is of early late Miocene age.

At all three sites, methane concentrations increased with depth, ranging from 5 to 29,000 ppm at Site 991, from 2 to 81 ppm at Site 992, and from 6 to 18,000 ppm at Site 993. The methane/ethane ratios in samples range from 30 to 830, suggesting that there may be a contribution of thermogenic gas to the microbial methane pool.

Detailed pore-water profiles from Holes 991A and 993A, both of which are located on the flanks of the diapir, show that chloride concentrations increase at a rate of 2 mM/m. However, in Hole 992A, located on the crest of the diapir, the gradient is significantly less (~0.8 mM/m). Dissolved sulfate contents in interstitial-water samples from Hole 991A decrease linearly with increasing depth, declining to negligible concentrations at ~35.6 mbsf. At this depth there is a corresponding alkalinity maximum (26.88 mM) in the interstitial-water samples. Ammonium contents increase linearly with depth, passing through the base of the sulfate reduction zone without inflection. These profiles suggest active anaerobic methane oxidation. Variations in the interstitial pore-water gradients at Sites 992 and 993 may reflect pore-water movement, changes in the upward flux of methane, or re-equilibration after the upper sedimentary section was removed during slumping.

BACKGROUND AND OBJECTIVES

Approximately 20 large diapiric structures have been identified on the Carolina Rise (Fig. 1) that are known as the Carolina Rise Diapirs. The diapirs appear to originate from the base of the Carolina Trough (see Fig. 3, "Introduction" chapter, this volume) to as much as 12 km below sea level (Dillon et al., 1982; Hutchinson et al., 1982). The diapirs form a linear array along the eastern margin of the Carolina Trough. Many investigators think that the diapirs are probably salt cored; however, no direct sampling has definitively confirmed the presence of salt.

The Carolina Rise Diapirs breech the seafloor only within the scar of the Cape Fear Slide (Figs. 1, 2). The Cape Fear Slide is one of the largest and best documented continental margin slide features in the world (Popenoe et al., 1993). Deposits from this slide extend downslope at least 400 km (Popenoe et al., 1993). Its headwall scarp is more than 50 km wide and 120 m high and encircles the Cape Fear Diapir (Figs. 2, 3). Whether the diapir caused the slide or whether gas hydrate is involved in the sediment failure is unknown, but much discussed (Carpenter, 1981; Cashman and Popenoe, 1985; Popenoe et al., 1993; Schmuck and Paull, 1993).

An isolated topographic high occurs within the Cape Fear Slide Scar over the Cape Fear Diapir (Fig. 4). Much of the sole of the Cape Fear Slide and the Cape Fear Diapir is covered with a thin (0–2 m thick) drape of sediment (Figs. 3, 5). ^{14}C data from piston cores indicate that this sediment drape consists of Holocene sediment (Paull et al., 1996). A hiatus on the sole of the slide separates sediments that are younger than 14.5 ka from those that are older than 29 ka, suggesting that the slide was active during the last glacial sea-level lowstand.

Seismic reflection profiles from the Carolina Rise commonly contain a distinct BSR (Dillon and Paull, 1983). Although a BSR occurs within the general region of the Cape Fear Diapir, the continuity of the BSR is lost on the diapir's flanks (Fig. 6). Thus, the diapir apparently produced a "hole" in the regional gas hydrate field that is suspected to be related to slumping and/or emplacement of the diapir.

Sites 991, 992, and 993 are situated on the flanks and crest of the Cape Fear Diapir (Figs. 2, 5, 6) where sediments that may formerly have contained gas hydrate have been disturbed. At all of the sites, we planned to penetrate materials exposed on the sole of Cape Fear Slide.

Site 991 is near the upslope flank of the diapir. We intended to penetrate sediments deformed by the emplacement of the diapir, but not thought to be part of the diapir's core. One goal was to assess the process of re-equilibration of the sedimentary pore-water chemical gradients after a significant section of the rise has been removed. These strata were buried more than 100 m before being exhumed by slumping associated with the Cape Fear Slide. Thus, when the slide occurred, methane-bearing sediments were exposed on the seafloor. With time, sulfate will diffuse back into these sediments and oxidize the pore-water methane. Evaluating the process of re-equilibration to new, shallower conditions may provide great insight into the sensitivity of gas hydrate–bearing sediment to changes in physical conditions and to the dynamics of gas hydrate venting.

Site 992 is near the topographic crest of the diapir. We intended to penetrate sediments deformed by emplacement of the diapir.

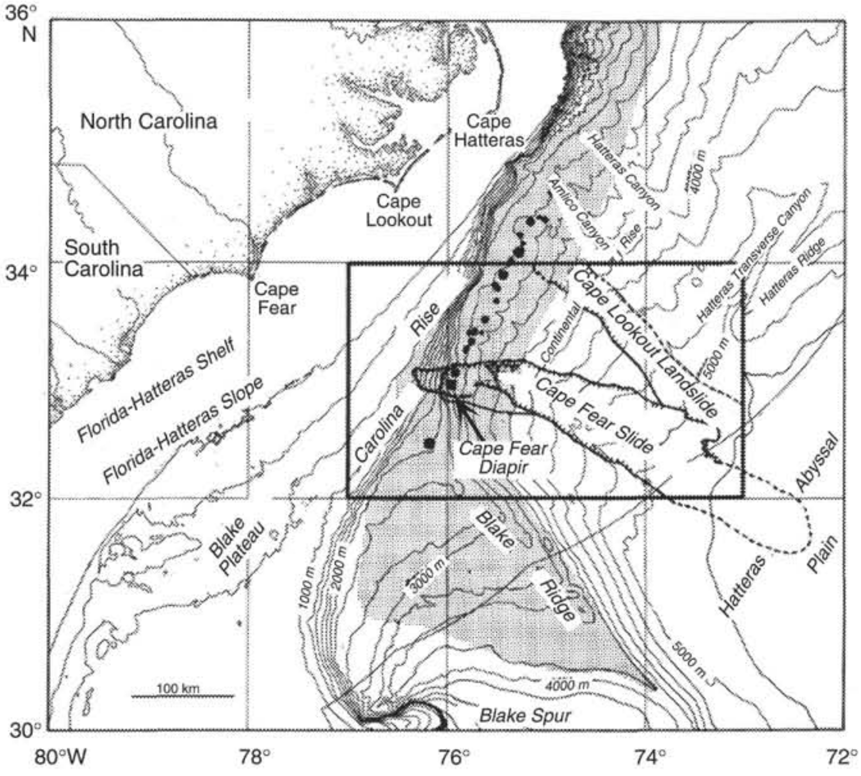

Figure 1. Regional map of the Cape Fear Diapir and Cape Fear Slide area (from Popenoe et al., 1993). The other Carolina Trough Diapirs are indicated by solid circles. The box indicates the area shown in Figure 2.

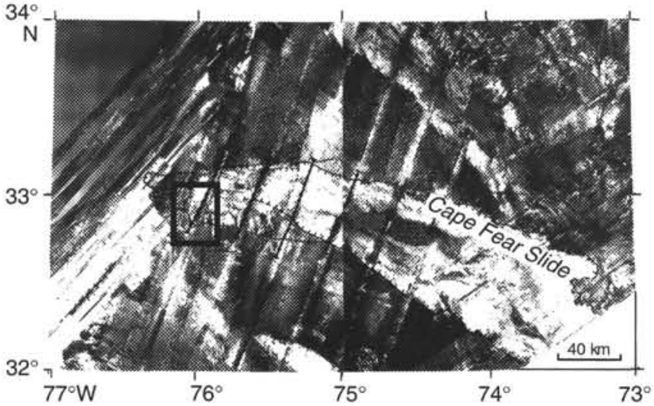

Figure 2. Geological long-range inclined asdic (GLORIA) side-scan sonar image of the area associated with the Cape Fear Diapir and the Cape Fear Slide (from Popenoe et al., 1993). The box indicates the area shown in Figure 3.

Whether these sediments are autochthonous or allochthonous is unclear.

Site 993 is on the southern flanks of the diapir in an area where side-scan sonar (Fig. 3), photography, and coring indicated that jointed, allochthonous materials of diverse Tertiary ages are exposed on the seafloor. These sediments apparently have come up from depth with the diapir.

The objectives of drilling at Sites 991, 992, and 993 are to (1) establish the tectonic, thermal, and hydrologic influence of the diapir on the regional gas hydrate field; (2) obtain samples beneath the sole of a major slump and materials transported upward by the diapir; (3) examine the nature of fluid and gas transport both through the sole of this major sediment scar and associated with the diapir itself; (4) examine the geochemical re-equilibration associated with the slumping; and (5) establish the nature of the core material of the diapir.

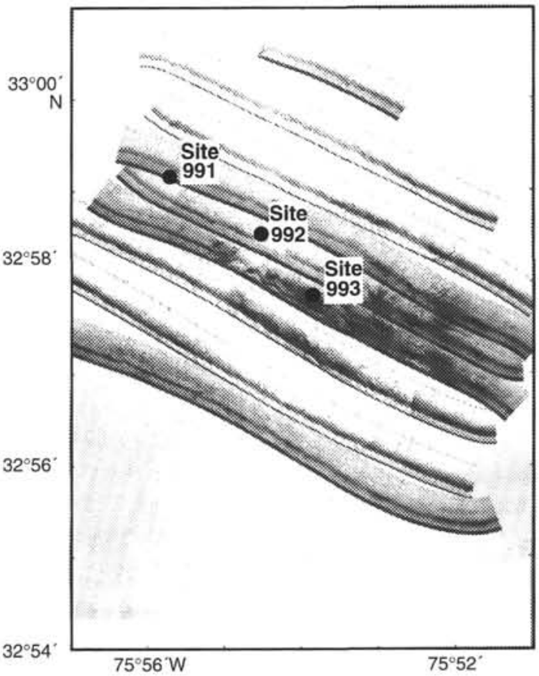

Figure 3. Side-scan sonar mosaic of nine approximately parallel north-looking 100-kHz sonograms collected with the Scripps Institution of Oceanography's deep-tow system (Speiss and Tyce, 1973) over the crest of the Cape Fear Diapir. Dark areas are more reflective. Note that the seafloor at Site 993 and to the southeast of Site 993 has a more reflective texture, whereas the seafloor to the northwest (around Sites 991 and 992) is more uniform and less reflective. Photographic surveys indicate that a melange of firm, jointed, and angular material occurs on the seafloor in the reflective area, whereas the seafloor is draped with sediment where the sonar images are less reflective. The area of the mosaic is shown in the box in Figure 2.

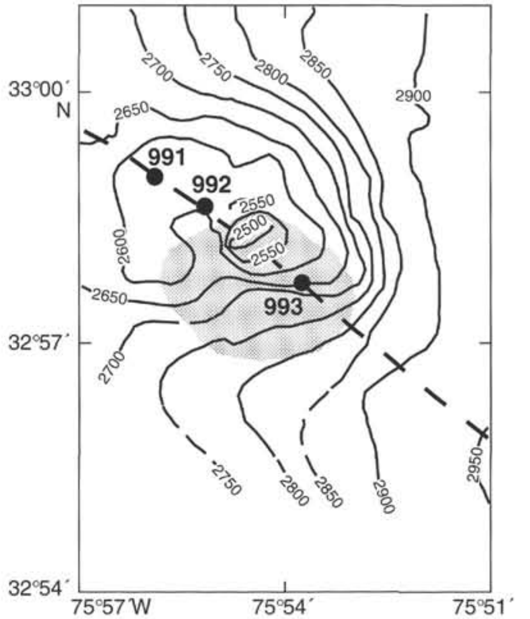

Figure 4. Locations of Sites 991, 992, and 993 are shown with respect to the bathymetry over the crest of the Cape Fear Diapir. Contours are based on a deep-tow survey. The area associated with reflective seafloor (Fig. 3) is marked with the shaded pattern. The location of the *JOIDES Resolution* profile, shown in Figures 5 and 6, is indicated with a bold dashed line.

OPERATIONS

Transit From Nova Scotia to Site 991

The ship departed from Halifax, Nova Scotia, Canada, at 1620 hr on 31 October 1995. The transit to Site 991 covered 1908 km in 95.6 hr at an average speed of 10.8 kt. The ship's course was initially set at 191° to cross roughly perpendicular to the east edge of the Gulf Stream rather than combat the current and to avoid the shipping lanes on the east coast of the United States. The ship's speed over ground was reduced to ~10.4 kt for 4 hr when crossing the Gulf Stream, and then a more direct course was taken. The main-shaft rpm was reduced again on 3 November in a Force 6–7 gale to reduce spray over the bow in heavy seas with 15-ft waves and 40-kt winds.

Hole 991A (Prospectus Site CFD-5)

An 83-km seismic survey was run in 6.8 hr at 6.0 kt over Sites 991, 992, and 993 and the Cape Fear Slide. Accurate positioning throughout Leg 164 was aided by the use of a differential Global Positioning System (GPS). The ship returned to the GPS coordinates for Site 991, and a Datasonics 354M commandable recall beacon was dropped at 0022 hr on 5 November (all Leg 164 drill sites were in the U.S. Eastern Time Zone; ship time, therefore, is equivalent to Universal Time Coordinated −5 hr). Hole 991A was spudded at 0835 hr on 5 November (Table 1). The water depth was measured as 2567.5 m below sea level (mbsl), based on recovery of the mudline in Core 164-991A-1H. APC Cores 164-991A-1H through 6H were taken from 0 to 56.6 mbsf seafloor, with 58.66 m recovered (103.6% recovery). The cores were relatively dry and well compacted and were not gassy. They contained a minor amount of H_2S as follows: 2 ppm at Core 164-991A-1H, 10 ppm at Core 3H, 22 ppm at Core 5H, and 20 ppm at Core 6H. There were no gas voids and little extrusion from the liner ends. Coring was halted for 0.5 hr for repairs when the forward core winch had an intermittent electrical control problem that caused it to jump at times. Hole 991A was terminated after Core 164-991A-6H, and the bit was pulled above the seafloor at 1418 hr on 5 November.

Hole 991B

The ship was moved 10 m south, and Hole 991B was spudded at 1507 hr on 5 November. The seafloor was assumed to be at 2567.5 mbsl, based on offset Hole 991A. The hole was washed to 10.0 mbsf for the first PCS run. Core 164-991B-1P was taken from 10.0 to 11.0 mbsf. A push-in type shoe and basket catcher were used. When retrieved, the PCS ball valve had closed, and the pressure chamber held 2550 psi when first checked. The pressure decreased slowly to 2270 psi in 2 min. Hydrostatic pressure was calculated at 3804 psi; therefore, some formation pressure was trapped. No core was recovered and it appeared that none entered the PCS catcher. The hole was drilled ahead from 11.0 to 50.0 mbsf, and Core 164-991B-2P was taken from 50.0 to 51.0 mbsf. A push-in type shoe and basket catcher were again used. A 104-cm core of moderately compacted green-gray clay was recovered, but a pressure of only 64 psi was trapped. The core barrel was jammed full, and the basket core catcher was partially broken off. The FWS was run for the first time at 51.0 mbsf and recovered 46 mL of water. Hole 991B was then terminated, and the bit was pulled above the seafloor at 1953 hr on 5 November.

Hole 992A (Prospectus Site CFD-6)

The 4.3-km move in dynamic positioning (DP) mode required 4 hr. The location of Site 992 was moved to the shipboard seismic line at 32° 58.5317′N, 75° 54.9968′W. After a water core, Hole 992A was spudded at 0210 hr on 6 November. The seafloor was estimated to lie at 2586.9 mbsl. Cores 164-992A-1H through 6H were taken from 0 to 50.3 mbsf, with a total of 50.3 m cored and 52.62 m recovered (104.6% average recovery). Hole 992A was terminated, and the bit was pulled above the seafloor at 0640 hr on 6 November.

Hole 993A (Prospectus Site CFD-7)

The ship was moved 2.8 km in DP mode in 2.75 hr. A Datasonics 354M beacon (S/N 778, 16.0 kHz) was dropped at 0849 hr on 6 November. The beacon drifted ~100 m north in the Gulf Stream current. After several water cores, the bit was run in to feel for bottom on the sloping diapir and slide area. Hole 993A was spudded at 1345 hr on 6 November. The 12-kHz precision depth recorder (PDR) indicated a water depth of 2616.5 mbsl; however, the seafloor was at 2641.8 mbsl, based on recovery of the mudline. Core 164-993A-1H was rejected in hard, dry clay, and a 1.9-m stroke was assumed, based on the 1.88-m recovery. The Adara APC temperature shoe was used to measure water temperature near the seafloor (3.1°C). Cores 164-993A-2X through 6X were taken from 1.9 to 51.9 mbsf, with 50.0 m cored and 43.81 m recovered (87.6% average recovery). Hole 993A was terminated, and the bit was pulled above the rotary table at 0020 hr on 7 November.

LITHOSTRATIGRAPHY

Introduction

Short holes were drilled at Sites 991, 992, and 993 on the crest and flanks of the Cape Fear Diapir (see "Background and Objectives" section, this chapter) with excellent recovery in Holes 991A, 992A, and 993A (Figs. 7–9). The lithostratigraphy of each of these holes is described separately below.

Site 991

Hole 991A was drilled to a depth of 56.6 mbsf, and 58.7 m of sediment was recovered. The sedimentary section that was recovered is divided into three major lithologic units: I, II, and III (Fig. 7). Large intervals of the cored section are characterized by structures indicative of soft-sediment deformation and large clay clasts.

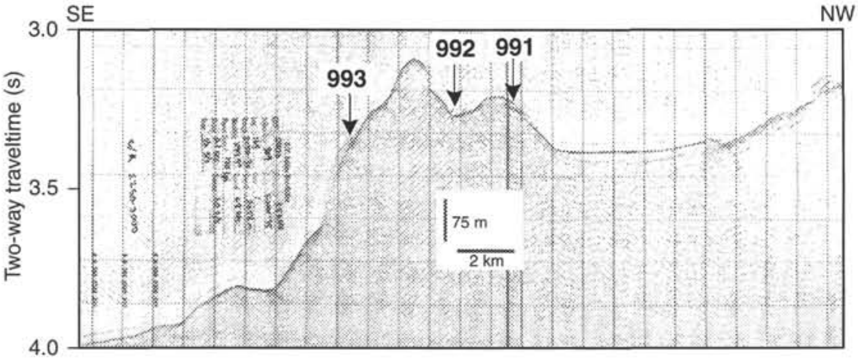

Figure 5. A 3.5-kHz profile over the Cape Fear Diapir showing the locations of Sites 991, 992, and 993. The location of the profile is indicated in Figure 4.

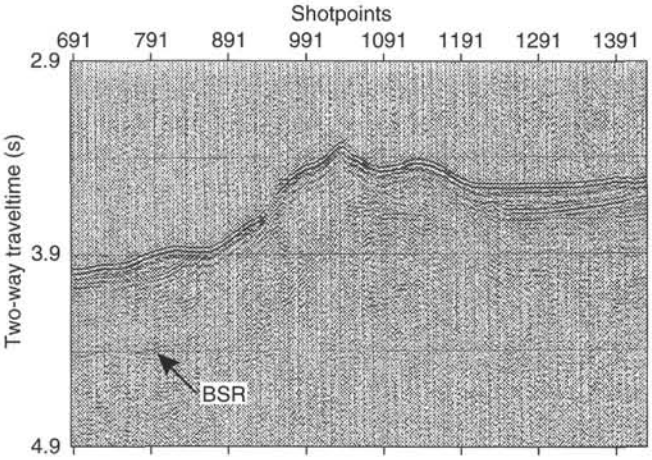

Figure 6. Seismic reflection profile over the crest of the Cape Fear Diapir showing the relationship to the headwall scar of the Cape Fear Slide. The location of the profile is indicated in Figure 4.

Unit I

Interval: 164-991A-1H-1, 0 cm, through 1H-2, 55 cm
Age: late Pleistocene to (?)Holocene
Depth: 0–2.05 mbsf

Unit I consists predominantly of gray nannofossil-rich clay to nannofossil clay with a minor component of silt. This unit is divided into two subunits to discriminate the distinctive thin, brownish colored section at the top of the unit.

Subunit IA

Subunit IA extends from the seafloor to a depth of 0.04 mbsf (interval 164-991A-1H-1, 0 cm, through 1H-1, 4 cm) and consists of a thin (4 cm) bed of reddish brown (5Y 5/4), foraminifer-bearing nannofossil-rich clay with abundant silt. The base of this subunit is sharp. The exact age of Subunit IA is uncertain, but may be Holocene.

Subunit IB

Subunit IB extends from the base of Subunit IA at 0.04 mbsf to 2.05 mbsf (interval 164-991A-1H-1, 4 cm, through 1H-2, 55 cm) and consists of gray to greenish gray (5YR 6/1 to 5GY 5/1) nannofossil-rich silty clay. Interval 164-991A-1H-1, 4 cm, through 1H-2, 20 cm (0.04–1.70 mbsf), is homogeneous; however, foraminifers and pteropods become increasingly abundant downward through interval 164-991A-1H-2, 20 cm, through 1H-2, 55 cm. This lower interval has the appearance of a normally graded bed and has a sharp, irregular lower contact. The carbonate content at the top of this subunit is 38.0 wt% (see "Organic Geochemistry" section, this chapter).

Table 1. Coring summary for Site 991/992/993.

Core	Date (Nov. 1995)	Time (UTC)	Depth (mbsf)	Length cored (m)	Length recovered (m)	Recovery (%)
164-991A-						
1H	5	1340	0.0–9.1	9.1	8.99	98.8
2H	5	1440	9.1–18.6	9.5	9.63	101.0
3H	5	1520	18.6–28.1	9.5	9.97	105.0
4H	5	1655	28.1–37.6	9.5	9.95	104.0
5H	5	1745	37.6–47.1	9.5	9.96	105.0
6H	5	1830	47.1–56.6	9.5	10.06	105.9
Coring totals				56.6	58.56	103.4
164-991B-						
1P	5	2045	10.0–11.0	1.0	0.00	0.0
2P	5	2300	50.0–51.0	1.0	1.04	104.0
Coring totals				2.0	1.04	52.0
164-992A-						
1H	6	0725	0.0–2.8	2.8	2.77	98.9
2H	6	0805	2.8–12.3	9.5	10.02	105.5
3H	6	0855	12.3–21.8	9.5	10.04	105.7
4H	6	0930	21.8–31.3	9.5	9.89	104.0
5H	6	1020	31.3–40.8	9.5	9.95	105.0
6H	6	1100	40.8–50.3	9.5	9.95	105.0
Coring totals				50.3	52.62	104.6
164-993A-						
1H	6	1900	0.0–1.9	1.9	1.88	98.9
2X	6	2315	1.9–13.8	11.9	9.76	82.0
3X	6	0100	13.8–23.0	9.2	9.81	106.0
4X	6	0225	23.0–32.6	9.6	9.68	101.0
5X	6	0330	32.6–42.2	9.6	9.50	98.9
6X	7	0045	42.2–51.9	9.7	5.07	52.2
Coring totals				51.9	45.70	88.1

Notes: UTC = Universal Time Coordinated. An expanded version of this coring summary table that includes lengths and depths of sections and sampling comments is included on CD-ROM in the back pocket of this volume.

Unit II

Interval: 164-991A-1H-2, 55 cm, through 6H-1, 56 cm
Age: early Pliocene to late Pleistocene
Depth: 2.05–47.66 mbsf

Unit II is a thick sequence of nannofossil-rich to nannofossil clay of variegated gray colors ranging through shades of gray (5Y 5/1), dark gray (5Y 4/1, 5Y 3/1), greenish gray (5GY 5/1, 5GY 6/1), olive gray (5Y 4/3, 5Y 4/2, 5Y 5/3, 5Y 5/2, 5Y 6/2, 5Y 3/2), and, rarely, black (5Y 2.5/1) (Figs. 10–15). These sediments are generally smooth and homogeneous and range in consistency from very soft to stiff. The carbonate content (Fig. 15) ranges from 9.5 to 56.7 wt% and is quite variable throughout the unit (see "Organic Geochemistry" section, this chapter).

Several intervals of sediment are clay conglomerates formed by soft-sediment failure, deformation, and redeposition, as evidenced by abrupt changes in lithology and color; discordant stratal relationships between dipping laminae, beds, and contacts; small folds, plastic flowage, and faults; and the occurrence of clay clasts of various sizes

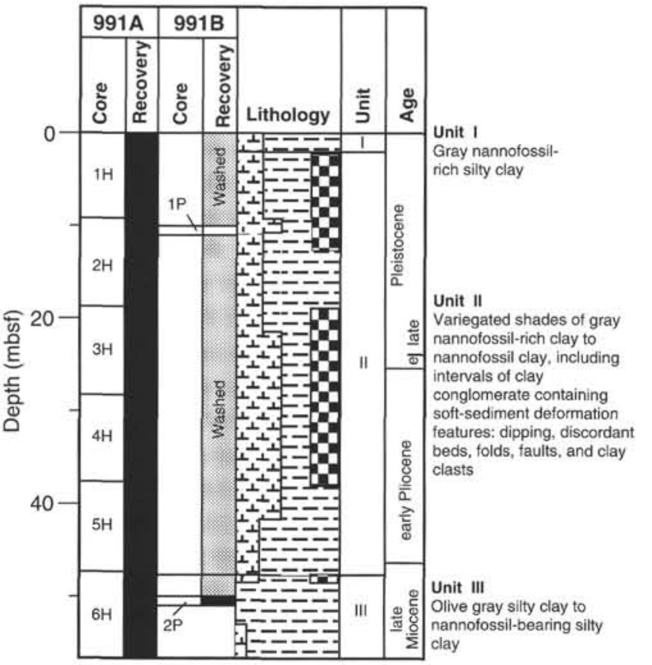

Figure 7. Composite stratigraphic section for Site 991 showing core recovery, a simplified summary of lithology, depth of lithologic unit boundaries, and age. The lithologic symbols are explained in Figure 2 of the "Explanatory Notes" chapter (this volume).

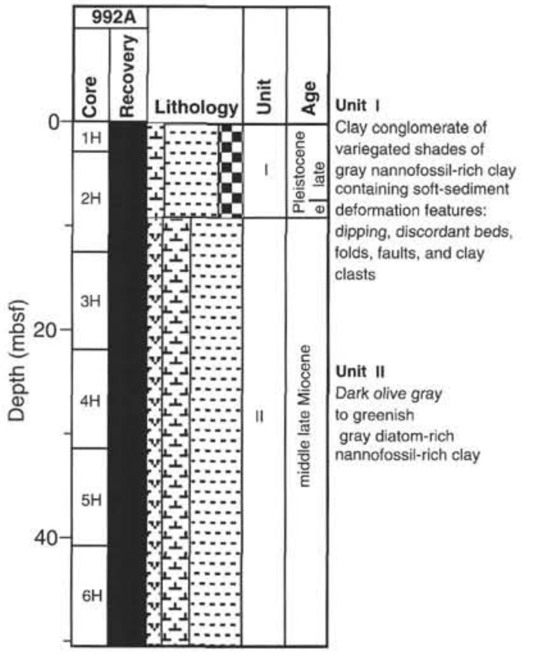

Figure 8. Composite stratigraphic section for Site 992 showing core recovery, a simplified summary of lithology, depth of lithologic unit boundaries, and age. The lithologic symbols are explained in Figure 2 of the "Explanatory Notes" chapter (this volume).

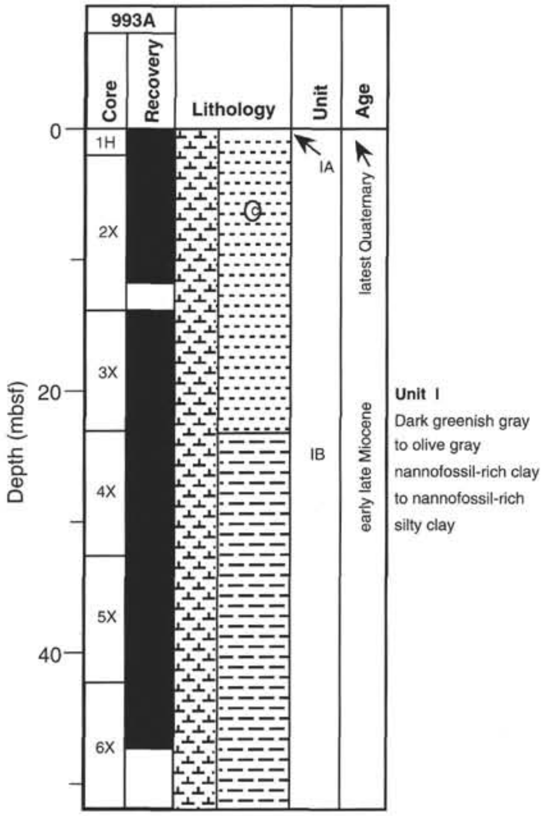

Figure 9. Composite stratigraphic section for Site 993 showing core recovery, a simplified summary of lithology, depth of lithologic unit boundaries, and age. The lithologic symbols are explained in Figure 2 of the "Explanatory Notes" chapter (this volume).

and colors (Figs. 10–12). Extensively deformed sediments comprise two major intervals within Unit II (intervals 164-991A-1H-2, 55 cm, through 2H-3, 57 cm [2.05–12.67 mbsf]; and 3H-1, 0 cm, through approximately 4H-CC, 24 cm [18.6–38.05 mbsf]) and a very thin interval (164-991A-5H-7, 55 cm, through 6H-1, 56 cm; 47.15–47.66 mbsf) at the base of Unit II (Fig. 7). These clay conglomerate intervals are separated by intervals of sediment that show little, or no, apparent disturbance.

Dipping color bands, laminae, beds, contacts, and burrows are ubiquitous throughout the extensively deformed intervals. Dips range from very slight to >60° (Figs. 10–12; see whole-core photographs in Section 4, this volume). Some groups of laminae and/or beds dip at various angles and directions and indicate discordant stratal relationships and truncated beds. Small-scale faults are rare and are indicative of shear or glide planes and brittle deformation. Plastic deformation or flowage of beds is common, and a few isoclinal or recumbent folds on the scale of centimeters occur (Figs. 10B, 11A). Some of these small folds and groups of dipping beds may represent portions of larger folds. Further evidence to suggest folding of the sediment, as well as faulting or shearing, is the deformed nature of some laminae and beds, which appear squeezed or stretched and have irregular boundaries that appear as "crenulated" patterns (Figs. 10B, 11).

Discrete clay clasts of various sizes, shapes, and colors are common to abundant in some intervals (Fig. 12). Clasts are round to angular in shape, as much as 15 cm in diameter, and commonly have undergone deformation. Both matrix-supported and clast-supported intervals occur. Some intervals of dipping beds also appear to be stacked, deformed clasts whose long dimensions are greater than the core width (e.g., Fig. 12). Shell fragments including echinoderms, pteropods, and other unidentified forms are rare.

Intervals with no apparent deformation or only minor evidence of deformation separate the highly deformed intervals described above (Fig. 7). The interval of homogeneous olive gray silty nannofossil-rich clay from 164-991A-2H-3, 57 cm, through 2H-CC, 27 cm (12.67–18.73 mbsf), shows no evidence of disturbance. The interval of homogeneous dark gray silty nannofossil-rich clay from 164-

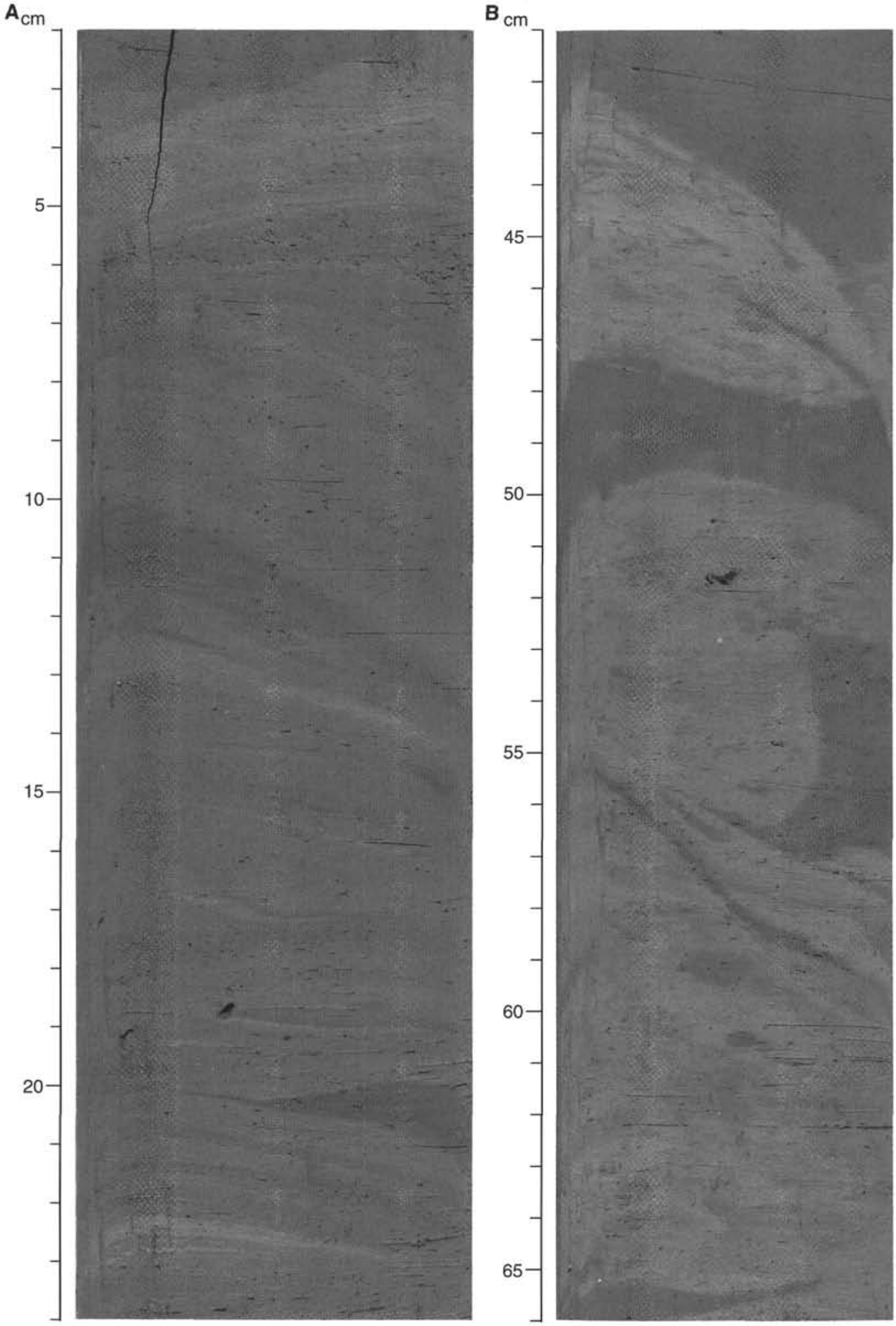

Figure 10. **A.** Deformed sediments of Unit II showing dipping, discordant, and truncated beds and laminae of variegated colors (interval 164-991A-1H-5, 2–24 cm). **B.** Deformed and folded beds and clasts of variegated colors in Unit II (interval 164-991A-1H-6, 41–66 cm).

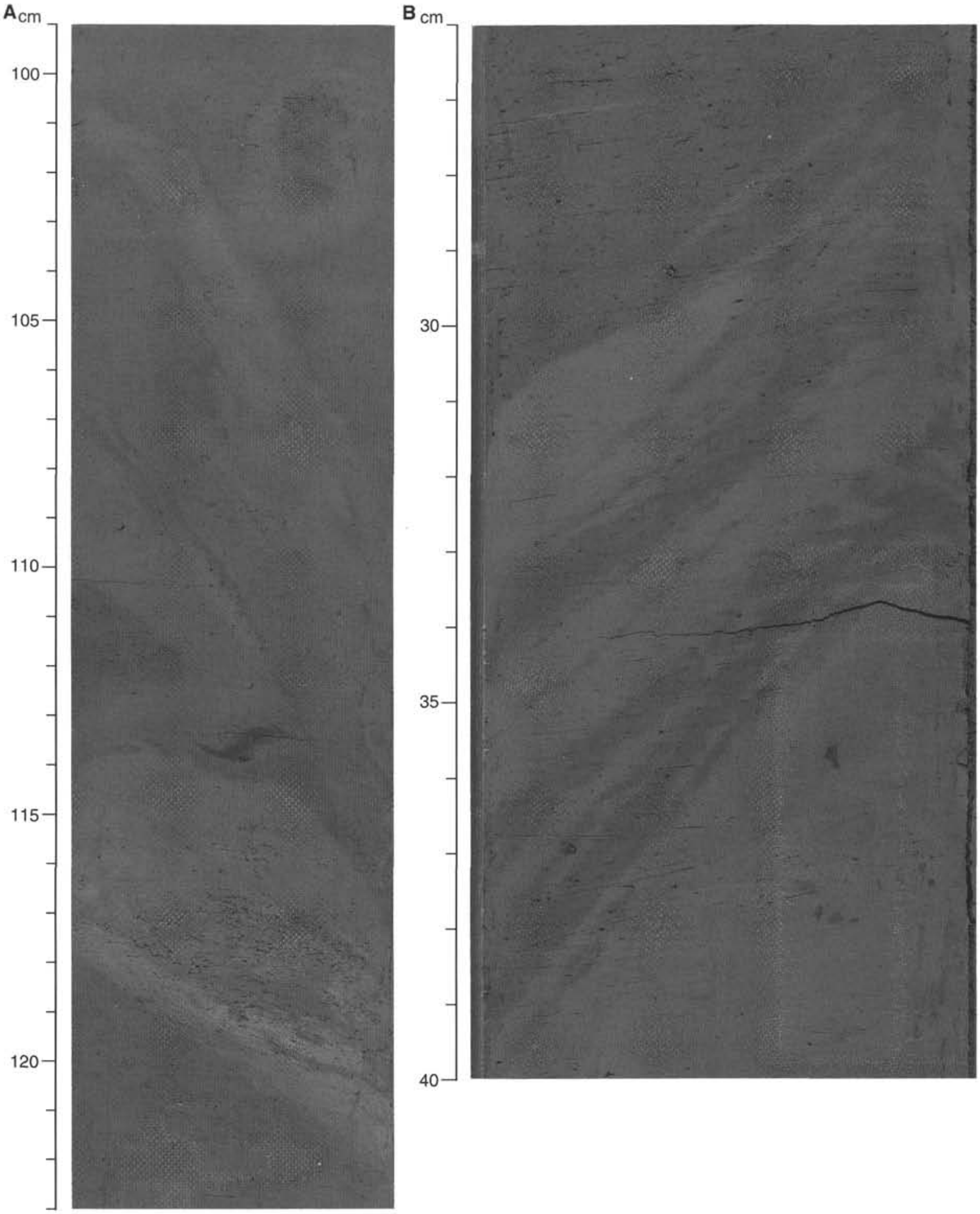

Figure 11. **A.** Deformed and folded beds and clasts of variegated colors in Unit II (interval 164-991A-2H-2, 99–123 cm). Note the recumbent fold from 107 to 114 cm. **B.** Dipping, deformed beds and laminae of variegated colors in Unit II (interval 164-991A-3H-4, 26–40 cm). Note the faulted or "crenulated" structures.

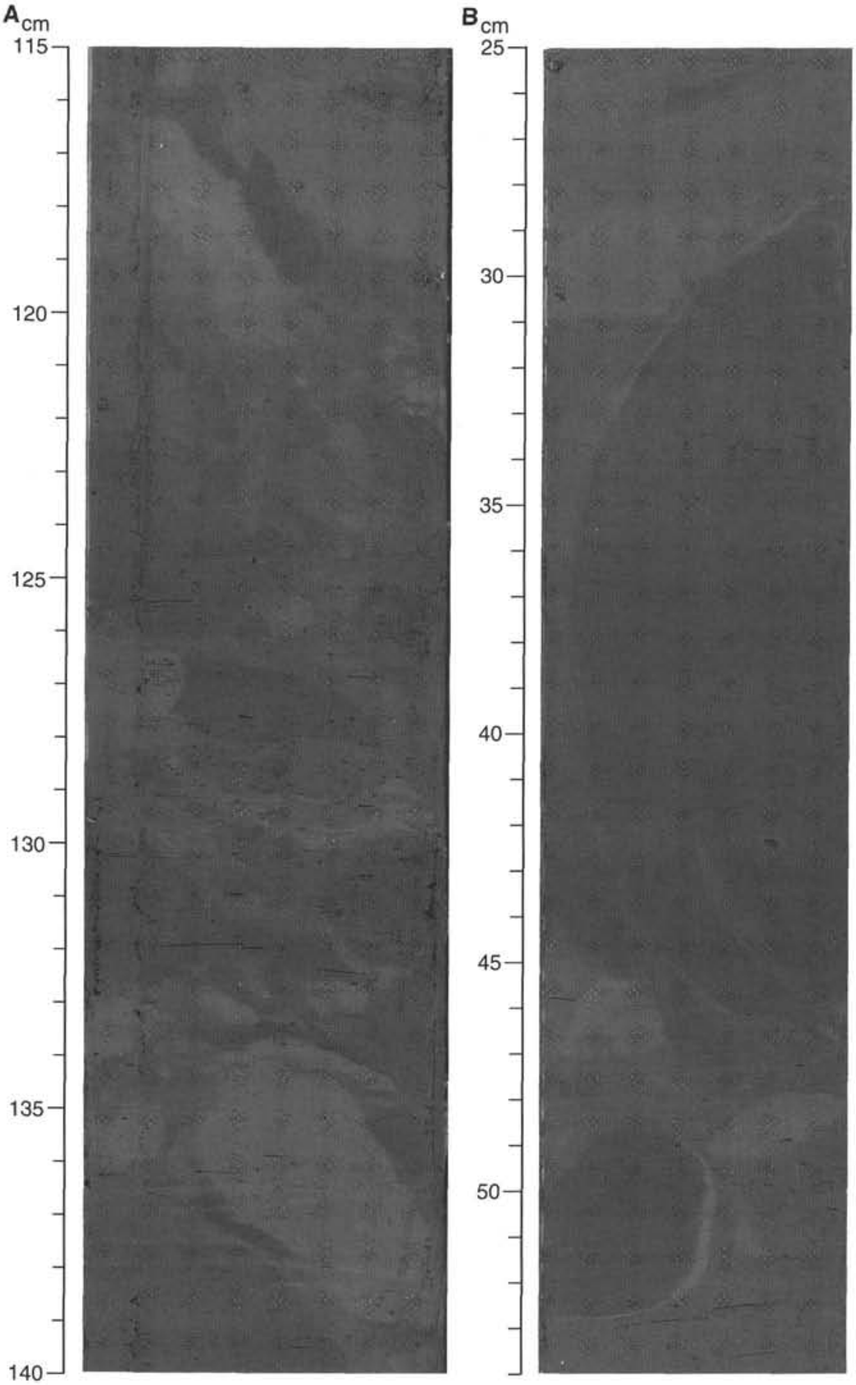

Figure 12. Clay clasts of various sizes, shapes, and colors in Unit II. **A.** Interval 164-991A-2H-1, 115–140 cm. **B.** Interval 164-991A-2H-2, 25–54 cm. Note the very large round clast from 28 to 47 cm.

991A-5H-1, 0 cm, through 5H-7, 55 cm (37.60–47.15 mbsf), is generally undeformed; however, some gently inclined beds occur in Section 164-991A-5H-2, and a dipping fault plane apparently occurs in interval 164-991A-5H-3, 90–100 cm. These undeformed intervals may represent sections of normal deposition that accumulated in place between events of soft-sediment deformation, or they may be undeformed sections within larger deformed intervals. Thus, some of the thicker undeformed intervals of sediment within Unit II may actually be large clasts or blocks as much as several meters thick, which span more than one core section.

Unit III

Interval: 164-991A-6H-1, 56 cm, through 6H-CC, 21 cm
Age: late Miocene
Depth: 47.66–57.16 mbsf

Unit III consists predominantly of dark olive gray, olive gray, and dark gray (5Y 3/2, 5Y 3/1, 5Y 4/2) silty clay that grades downward into nannofossil-bearing clayey silt and silty clay (Fig. 7), which also contains disseminated carbonate rhombs and minor pyrite. The top of

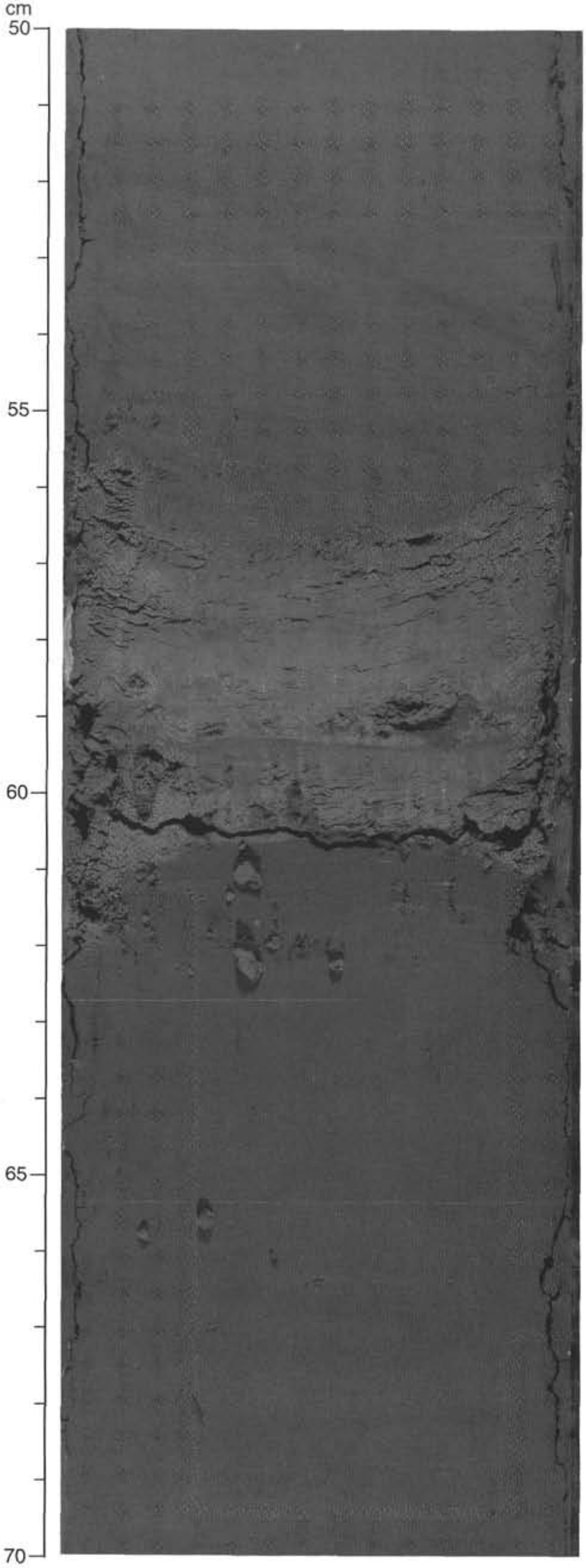

Figure 13. Contact between Units II and III at 56 cm (interval 164-991A-6H-1, 50–70 cm). Note the bed of carbonate-rich nannofossil clayey silt at the top of Unit III from 56 to 61 cm.

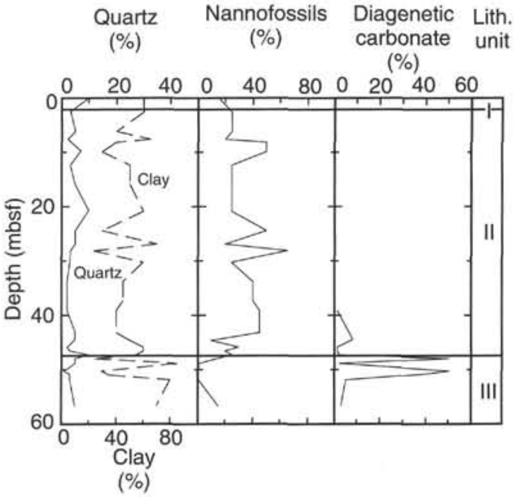

Figure 14. Plots of percentages of nannofossils, clay, quartz, and diagenetic carbonate, based on smear-slide estimates down Hole 991A.

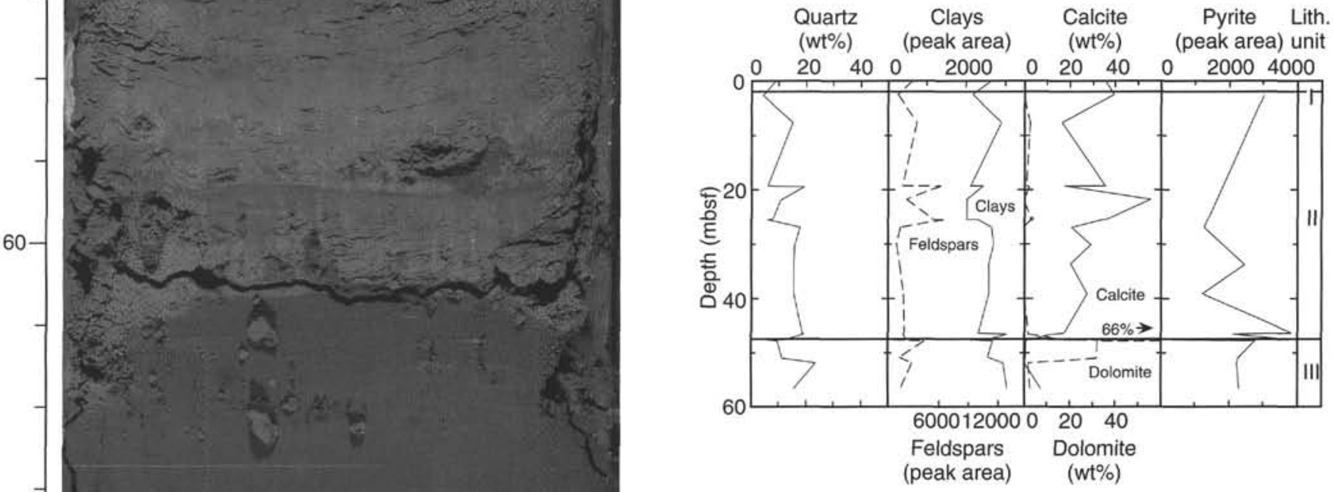

Figure 15. XRD analyses down Hole 991A plotted according to integrated peak intensities for clays, feldspars, and pyrite. Weight percentages for quartz, calcite, and dolomite are calculated using the method described in the "Explanatory Notes" chapter (this volume).

Unit III is marked by a 6-cm-thick bed (interval 164-991A-6H-1, 56–61 cm; 47.66–47.71 mbsf) of carbonate-rich nannofossil clayey silt (Fig. 16). The carbonate content is 77.1 wt% near the top of the unit (47.68 mbsf), but it rapidly decreases downhole to a minimum of 2.1 wt% at 51.83 mbsf (see "Organic Geochemistry" section, this chapter).

A steeply dipping, irregular contact occurs just below this carbonate-rich bed in the interval 164-991A-6H-1, 93–100 cm. A large clay clast occurs just above this angular contact. These features suggest that this uppermost portion of the unit has been affected by soft-sediment deformation, probably in response to the processes that emplaced the deformed section(s) of Unit II. Although this interval is apparently deformed, it has been included in Unit III because the lithology and age of the sediments are similar to those of the underlying undisturbed sediments in Unit III.

Sediment Composition Based on Smear-Slide and XRD Analyses

The mineralogy of bulk sediment from Hole 991A was determined by X-ray diffraction (XRD) analysis (Table 2) combined with routine visual estimates of dominant mineral and biogenic compo-

Table 2. Main diffraction peak areas and weight percentage proportions for minerals identified in samples from Holes 991A, 992A, and 993A.

Core, section, interval (cm)	Depth (mbsf)	Peak area									Quartz* (wt%)	Calcite* (wt%)	Dolomite* (wt%)
		Quartz (100)	Quartz (101)	Clay	Plagioclase	Aragonite (012)	Calcite	Dolomite	Siderite	Pyrite			
164-991A-													
1H-1, 5–6	0.05	3,310	12,213	2,637	2,634	2,478	15,974				9	35	0
1H-2, 109–110	2.59	2,374	5,651	2,171	1,036	4,139	17,068			3,018	4	39	0
1H-6, 19–20	7.69	5,057	21,635	2,912	3,202	892	9,445	2,836			15	16	3
3H-1, 67–68	19.27	3,216	8,347	2,109	1,588	4,169	16,039	1,124			6	36	1
3H-1, 80–81	19.40	5,222	27,252	2,441	5,784	957	9,956	2,390			19	18	2
3H-3, 28–29	21.88	4,252	14,950	2,018	1,984	2,617	21,184				11	55	0
3H-5, 88–89	25.48	3,690	11,038	2,010	4,888	2,358	16,109	2,986			8	36	3
3H-5, 90–91	25.50	1,931	8,385	2,315	6,071	3,863	15,681	3,001			6	34	3
3H-6, 86–87	26.96	4,485	25,388	2,649	1,326	1,269	11,198			1,265	18	21	0
4H-2, 59–60	30.19	5,367	22,417	2,721	940	1,258	14,000				16	29	0

Note: * = percentages (wt%) for quartz, calcite, and dolomite are calculated using the calibration curves described in the "Lithostratigraphy" section of the "Explanatory Notes" chapter (this volume).

Only part of this table is produced here. The entire table appears on the CD-ROM (back pocket).

nents from smear slides (see Section 5, this volume). Smear-slide observations show an overall good correspondence with the XRD data (Figs. 14, 15). Based on smear-slide studies and XRD peak positions of individual minerals, quartz, feldspars, aragonite, calcite, dolomite, pyrite, and undifferentiated clay minerals (see "Explanatory Notes" chapter, this volume) were identified as the major mineral components. The relative abundance of these minerals was determined from their peak areas (Fig. 15).

Downhole abundances of quartz and clay generally parallel each other (Fig. 15). Both exhibit minima at 25 mbsf, which corresponds to a hiatus between the lower Pliocene and the lower Pleistocene. Minima in quartz and clays also occur at 48 mbsf and correspond to a major change in lithology at the boundary between Units II and III. Feldspar abundance varies little downhole, but it does exhibit maxima at 20 and 26 mbsf; the latter maximum corresponds to the Pleistocene–Pliocene hiatus.

Aragonite and calcite abundances generally mirror quartz and clay minerals (Figs. 14, 15), but aragonite is absent below 30 mbsf. Variations in the aragonite and calcite are indicative of fluctuations in terrigenous influx (dilution), biogenic carbonate production, and/or carbonate dissolution. Calcite content generally decreases downhole, reaching a minimum at the base of Unit II (48 mbsf). The 5-cm-thick bed of carbonate-rich nannofossil clayey silt (interval 164-991A-6H-1, 56–61 cm; 47.66–47.71 mbsf) (Fig. 13), which marks the contact between Units II and III, is dominated by dolomite. The authigenic nature of this dolomite is confirmed by smear-slide studies of this bed, which show abundant rhombohedrally shaped crystals (Fig. 16). Minor amounts of dolomite are disseminated throughout the sediments above and below this bed.

The origin of the carbonate bed at the top of Unit III is uncertain. Petrographic observations indicate that dolomite may have replaced unidentified mineral grains that have the morphology of gypsum. However, no gypsum was recorded by XRD analyses. The occurrence of this carbonate horizon at the top of Unit III near the base of the deformed, displaced sediment section of Unit II, suggests that diagenesis may be related to fluid advection at the base of the deformed sediments. Alternatively, dolomite may have formed when this sediment was near the seafloor before deposition of Unit II.

Site 992

Hole 992A was drilled to a depth of 50.3 mbsf, and 52.6 m of sediment was recovered. The sedimentary section is divided into two major lithologic units (Fig. 8). Although the upper 9 m of the cored section consists of clay conglomerates formed by soft-sediment deformation processes, the majority of the section appears to be undisturbed hemipelagic sediments.

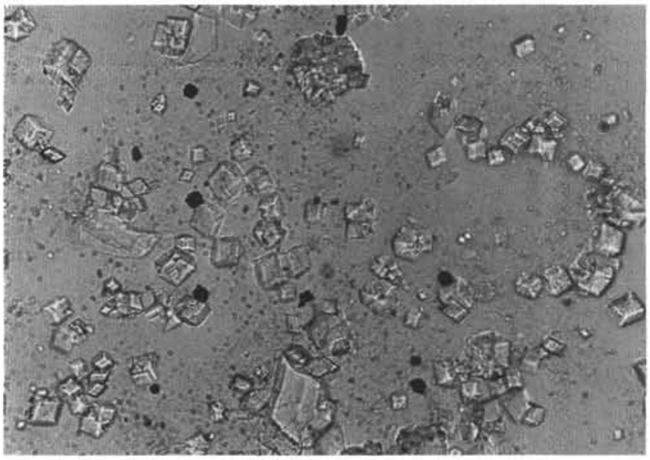

Figure 16. Photomicrograph of a smear slide showing authigenic dolomite, pyrite, and replacement of an unidentified mineral by dolomite (interval 164-991A-6H-1, 120 cm). Photomicrograph taken with a 25× objective.

Unit I

Interval: 164-992A-1H-1, 0 cm, through 2H-5, 30 cm
Age: Pleistocene to (?)Holocene
Depth: 0–9.10 mbsf

Unit I consists predominantly of a thick sequence of clay conglomerates composed of nannofossil-rich clays of variegated gray colors that have undergone soft-sediment deformation. This unit is divided into two subunits to discriminate the distinctive thin, brownish colored section at the top of the unit.

Subunit IA

Subunit IA extends from the seafloor to a depth of 0.04 mbsf (interval 164-992A-1H-1, 0 cm, through 1H-1, 4 cm) and consists of a very thin (4 cm) bed of brown (7YR 5/2) nannofossil-rich clay. Although this interval appears similar in color and composition to Subunits IA in Holes 991A and 993A, Subunit IA in this hole has a dipping basal contact and shows some indication of disturbance or deformation. Thus, this bed may be displaced (e.g., clay clast) and, as such, is part of the sediments of Subunit IB.

Subunit IB

Subunit IB extends from the base of Subunit IA at 0.04 mbsf to 9.10 mbsf (interval 164-991A-1H-1, 4 cm, through 2H-5, 30 cm) and

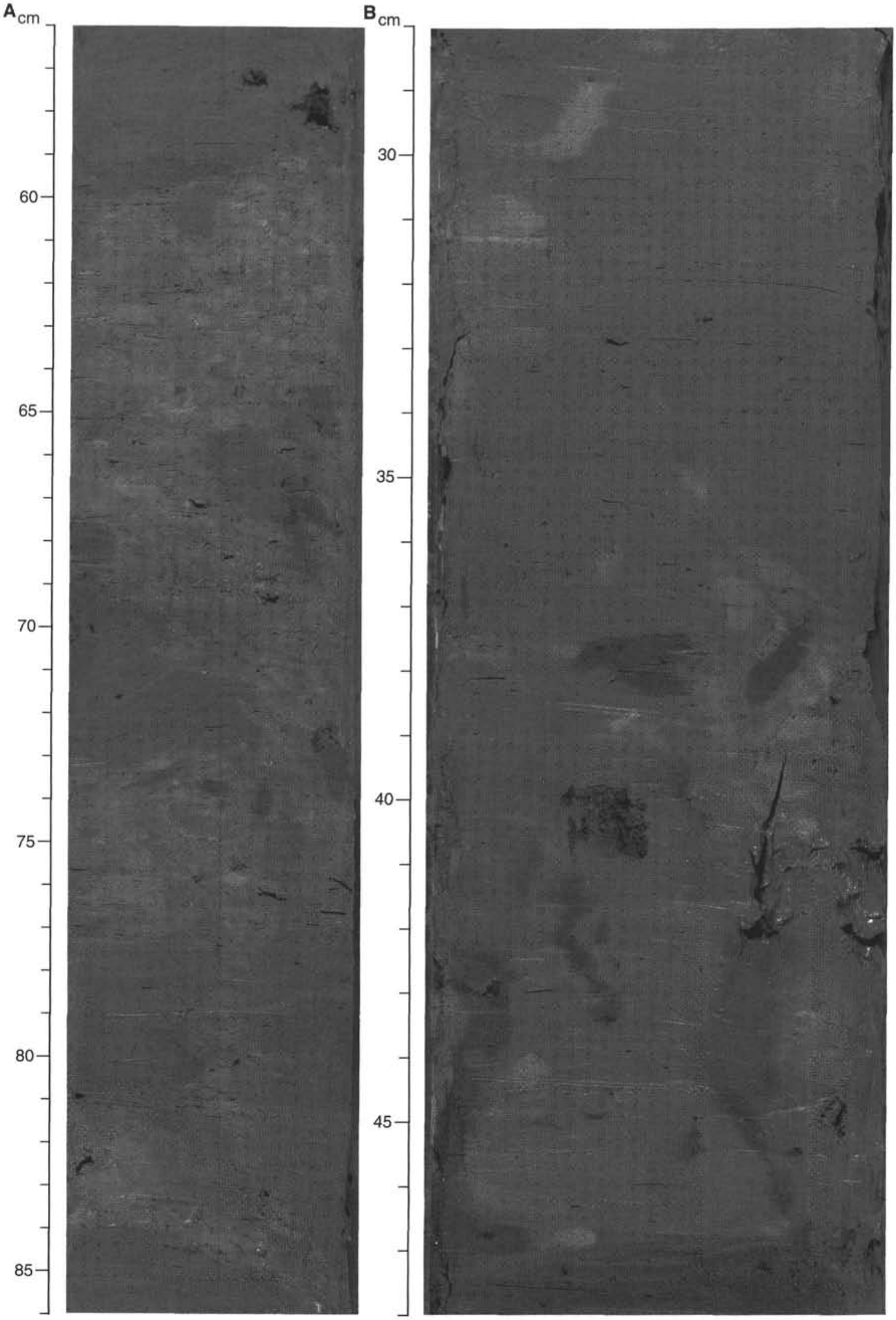

Figure 17. Clay clasts of various sizes, shapes, and colors in deformed sediments of Unit I. **A.** Interval 164-992A-1H-1, 56–86 cm. **B.** Interval 164-992A-2H-3, 28–48 cm.

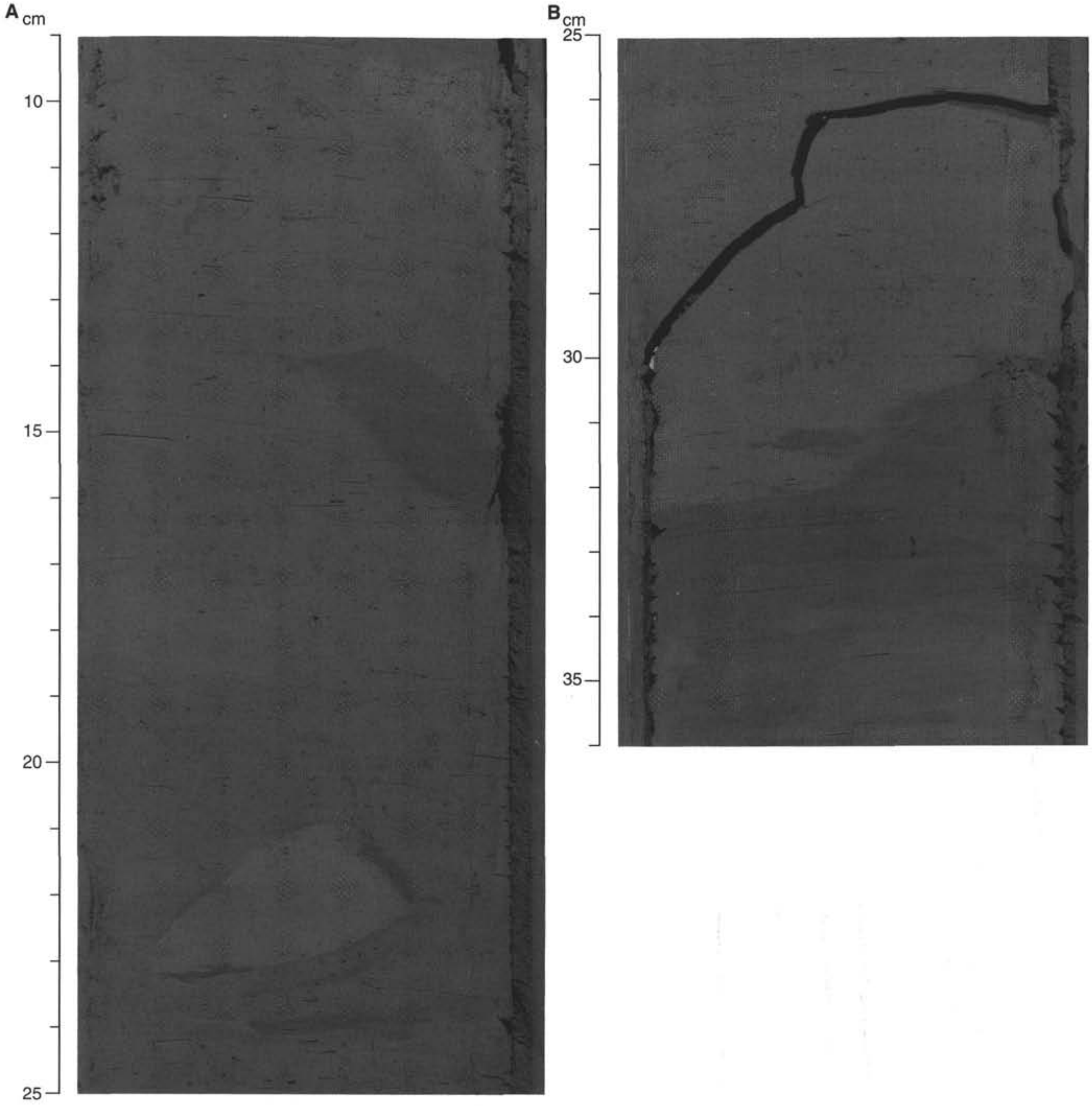

Figure 18. **A.** Clay clasts of various sizes, shapes, and colors in deformed sediments of Unit I (interval 164-992A-2H-5, 9–25 cm). **B.** Dipping, irregular contact separating the contrasting lithologies of Unit I (above) and Unit II (below) (interval 164-992A-2H-5, 25–36 cm).

consists of a thick sequence of clay conglomerates composed of nannofossil-rich clay of variegated gray colors ranging through shades of gray (5Y 5/1, N5, 5Y 7/1), dark gray (5Y 4/1), greenish gray (5GY 5/1), and olive gray (5Y 4/2, 5Y 5/2). These sediments are generally smooth and range in consistency from very soft to stiff. The carbonate content ranges from 24.6 to 66.9 wt% (see "Organic Geochemistry" section, this chapter).

Virtually all of the sediments throughout Subunit IB have been affected by soft-sediment failure, deformation, and redeposition as evidenced by abrupt changes in lithology and color; discordant stratal relationships between dipping laminae, beds, and lithologic contacts; small folds, plastic flowage, and faults; and the occurrence of clay clasts of various sizes and colors (Figs. 17, 18; see whole-core photographs in Section 4 of this volume). The base of Subunit IB is marked by an irregular, dipping contact and a distinct change in color and lithology (Fig. 18B).

Groups of color bands, laminae, beds, contacts, and burrows dip at various angles (up to ~50°) and directions and show discordant stratal relationships and truncated beds. Small-scale faults indicate shear or glide planes and brittle deformation. Plastic deformation or flowage of beds is common, and small isoclinal or recumbent folds on the scale of centimeters are rare. Some groups of dipping beds may represent portions of larger folds. Further evidence of folding, as well as faulting or shearing, is the occurrence of deformed laminae and beds, which appear squeezed or stretched and have irregular boundaries with "crenulated" patterns. Small intervals containing clastic injections of clay or foraminifer/pteropod ooze are rare.

Discrete clay clasts of various sizes, shapes, and colors are common to abundant in some intervals; both matrix-supported and clast-supported intervals occur (Figs. 17, 18A). Clasts are round to angular in shape, and some have undergone deformation. Discrete clasts as much as several centimeters in diameter are observed; however, some of the intervals of dipping beds may be stacked clasts, whose long dimensions are greater than the core width. Shell fragments including echinoderms, pteropods, and other unidentified fragments are rare.

Unit II

Interval: 164-992A-2H-5, 30 cm, through 6H-CC, 31 cm
Age: middle late Miocene
Depth: 9.10–50.75 mbsf

Unit II consists of undisturbed, rather homogeneous diatom- and nannofossil-rich clay with colors of dark olive gray (5Y 3/2, 5Y 4/2), dark greenish gray (5GY 4/1), and dark gray (5Y 4/1). Carbonate contents are relatively low (7.7 to 17.2 wt%; see "Organic Geochemistry" section, this chapter). Disseminated carbonate rhombs are abundant in the uppermost portion of the unit but are rare to absent below 21 mbsf. Bioturbation is slight to absent in the upper part of the unit but becomes extensive below ~33 mbsf.

Sediment Composition Based on Smear-Slide and XRD Analyses

The major sediment components, identified by a combination of smear-slide (see Section 5, this volume) and XRD analyses (Table 2), are nannofossils, diatoms, quartz, clay, calcite, and dolomite (Figs. 19, 20). Foraminifers, radiolarians, pyrite, feldspars, and glauconite occur as minor components. No aragonite was present below 5 mbsf.

After sharp increases in the upper meter of the hole, quartz and clay show relatively steady abundances down the sediment column (Figs. 19, 20). This trend is generally mirrored by the calcite content. However, calcite reaches a minimum at ~11 mbsf, which is caused by the formation of authigenic dolomite at the expense of biogenic carbonate. This diagenetic zone corresponds to an unconformity between Pleistocene and Miocene sediments at the boundary between Units I and II. Nannofossil and diatom abundances also exhibit a marked downhole increase in Unit II and correspond to a change in lithology between Units I and II. Pyrite occurs in trace amounts within Unit I but is pervasive throughout Unit II. The association of increased authigenic dolomite at the top of Unit II, just beneath the base of deformed sediments of Unit I, suggests that carbonate mineralization occurred before, or in response to, emplacement of deformed sediments.

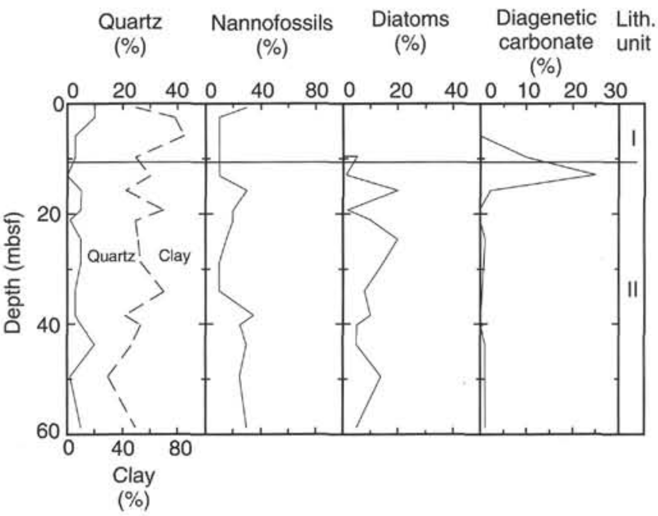

Figure 19. Plots of percentages of nannofossils, diatoms, clay, quartz, and diagenetic carbonate, based on smear-slide estimates down Hole 992A.

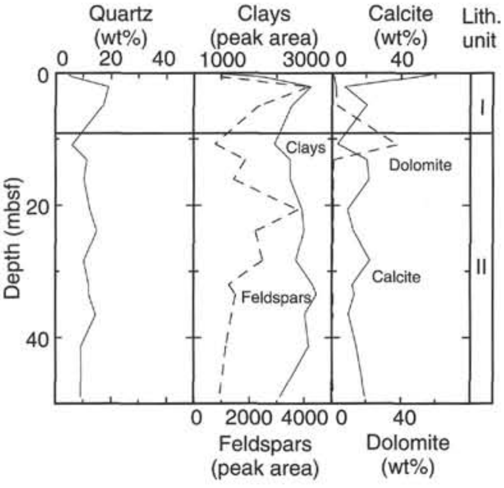

Figure 20. XRD analyses down Hole 992A plotted according to integrated peak intensities for clays and feldspars. Weight percentages for quartz, calcite, and dolomite are calculated using the method described in the "Explanatory Notes" chapter (this volume).

Site 993

Hole 993A was drilled to a depth of 51.9 mbsf and recovered 43.8 m of sediments (Fig. 9). The sedimentary section recovered is largely homogeneous nannofossil-rich clay and, therefore, comprises only one lithostratigraphic unit.

Unit I

Interval: 164-993A-1H-1, 0 cm, through 6X-CC, 20 cm
Age: early late Miocene to late Pleistocene/(?)Holocene
Depth: 0–47.27 mbsf

Unit I consists predominantly of gray nannofossil-rich clay. Unit I is divided into Subunits IA and IB to discriminate the distinctive thin, brownish colored section (Subunit IA) at the top of the unit from the remainder of the section (Fig. 9).

Subunit IA

Subunit IA extends from the seafloor to a depth of 0.06 mbsf (interval 164-993A-1H-1, 0 cm, through 1H-1, 6 cm) and consists of a thin (6 cm) bed of olive brown (2.5Y 4/4) nannofossil clay. The base of this subunit is sharp. The exact age of Subunit IA has not yet been determined, but it is latest Quaternary (see "Biostratigraphy" section, this chapter).

Subunit IB

Subunit IB extends from the base of Subunit IA at 0.06 mbsf to 47.27 mbsf (interval 164-993A-1H-1, 6 cm, through 6X-CC, 20 cm) near the base of the hole and consists of dark greenish gray (5GY 4/1), olive gray (5Y 4/2), and dark gray (5Y 4/1) nannofossil-rich clay that grades downward into nannofossil-rich silty clay below ~23.0 mbsf. Carbonate contents range from 11.3 to 23.2 wt% (see "Organic

Geochemistry" section, this chapter). Pyrite and carbonate rhombs are disseminated throughout the section. The abundance of carbonate rhombs is typically 1%–5%. Bioturbation is generally slight to rare.

Interval 164-993A-2X-3, 60–93 cm (3.60–3.93 mbsf), comprises a lithified, gray (5Y 5/1) carbonate nodule surrounded by calcareous silty clay (Fig. 21). Many smaller (<1 cm diameter) similar nodules are disseminated in the interval directly below this nodule (interval 164-993A-2X-3, 93–140 cm; 3.93–4.40 mbsf).

Sediment Composition Based on Smear-Slide, Thin-Section, and XRD Analyses

Nannofossils (15%–20%) and clay (60%–70%) are the dominant sediment components at Hole 993A (Figs. 22, 23; Table 2; see Section 5, this volume). Foraminifers, biogenic silica, quartz, feldspars, pyrite, and authigenic carbonate contribute to the sediment composition in minor amounts (<5%). The downhole abundances of the sediment components are rather uniform with overall slight increases of quartz, clay, and feldspar. The sharp increase of dolomite, accompanied by a marked decrease in all other components, is caused by a 33-cm-thick carbonate nodule in interval 164-993A-2X-3, 60–93 cm (3.60–3.93 mbsf) (Fig. 21). Thin-section analysis shows that this nodule is characterized by an equigranular, microcrystalline (10 µm) dolomite cement (Fig. 24) that has replaced much of the original sediment. Quartz, clay minerals, and minor amounts of pyrite are disseminated throughout the nodule. Unlike Sites 991 and 992, the diagenetic zone in this core is neither associated with a lithologic contact, nor a hiatus. The association of the intergranular dolomite cement and pyrite suggests an anaerobic origin for cementation (Berner, 1984; Jorgensen, 1987). Siderite occurs in trace amounts at 10 m, then increases in abundance downhole. Siderite content at the base of the hole is estimated to be less than 5% of the sediment.

Discussion of Sites 991, 992, and 993

Sites 991, 992, and 993 are on the flanks and crest of the Cape Fear Diapir (see "Background and Objectives" section, this chapter). A 3.5-kHz PDR profile across the sites (Fig. 5) shows that Site 991 is on the landward flank of the diapir several tens of meters above the surrounding seafloor. Although Site 992 is on the crest of the diapir, it is in a saddle at a location that is bathymetrically deeper than Site 991. Site 993 is on the steep seaward flank of the diapir. All three sites are several tens of meters above the surrounding seafloor, which has been affected by the Cape Fear Slide. Sediments on the flanks and crests of diapirs, such as this one, generally are subject to failure because of the steep slopes associated with these features (e.g., Fig. 5). Such sediment failure generates localized mass-transport deposits, usually slumps and debris flows.

Unit II and the uppermost interval of Unit III in Hole 991A, as well as Unit I in Hole 992A, clearly contain intervals of clay conglomerates composed of extensively disturbed sediments that have undergone soft-sediment deformation during failure and subsequent deposition by mass-transport processes (e.g., slumping, sliding, and debris flow). The occurrence of clay clasts and blocks of various sizes suggests deposition by debris flows, whereas the occurrence of small folds, and possibly larger folds of various scales, suggests slumping. The number and timing of mass-wasting events represented at each site is uncertain. Hole 991A has three or more discrete mass-transport zones of different ages (Miocene to Pleistocene) punctuated by seemingly undisturbed sediment intervals, and there are apparently biostratigraphic reversals of age (i.e., older over younger sediments; see Fig. 25) that confirm multiple mass-transport events.

The mass-transport deposits comprising Unit I in Hole 992A are thinner than those in Hole 991A and are only Pleistocene in age. This may reflect the position of Hole 992A on the diapir summit, where sediment failure and removal may have been more prevalent. Consequently, much of the section between the upper Miocene and the

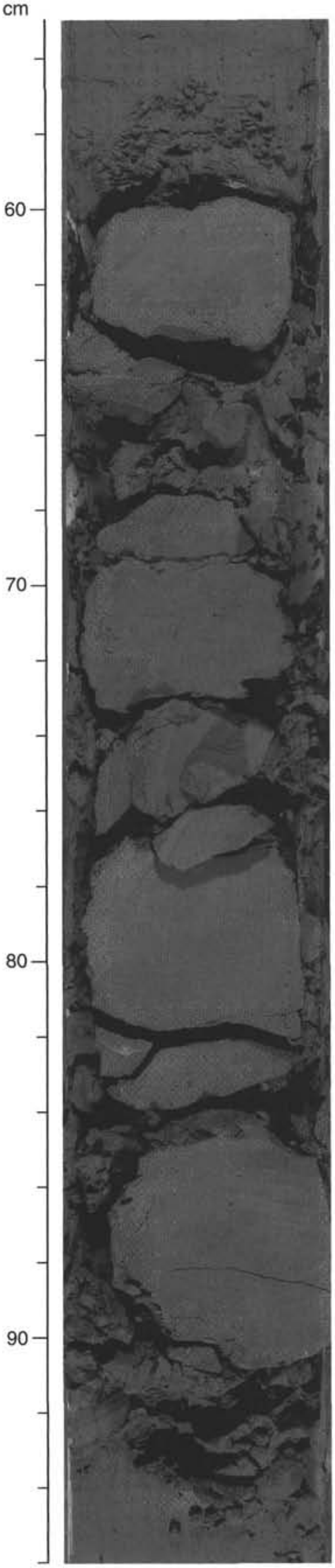

Figure 21. Lithified carbonate nodule (interval 164-993A-2X-3, 55–96 cm).

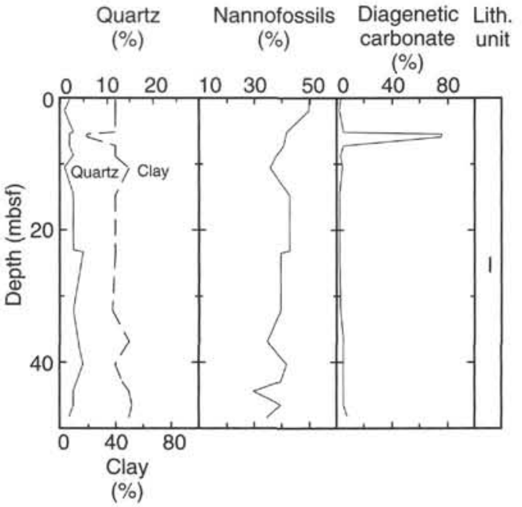

Figure 22. Plots of percentages of nannofossils, quartz, clay, and diagenetic carbonate, based on smear-slide estimates down Hole 993A.

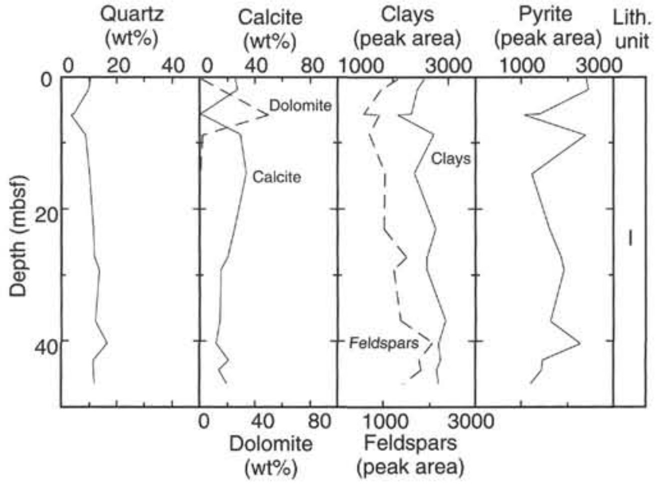

Figure 23. XRD analyses down Hole 993A plotted according to integrated peak intensities for clays, feldspars, and pyrite. Weight percentages for quartz, calcite, and dolomite are calculated using the method described in the "Explanatory Notes" chapter (this volume).

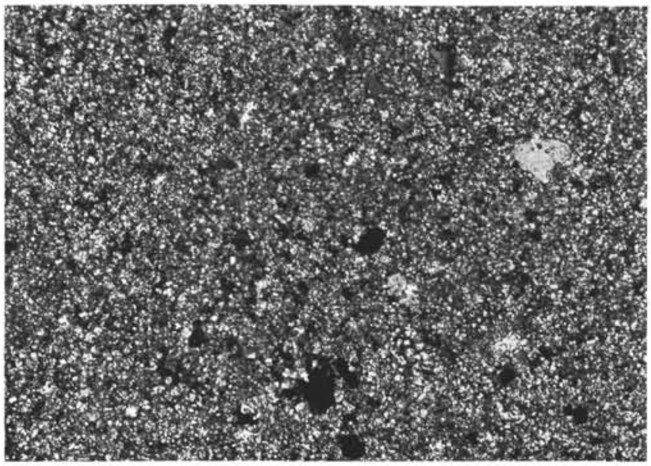

Figure 24. Photomicrograph of a thin section from the bed of carbonate-rich nannofossil clayey silt at the top of Unit III (interval 164-993A-2X-3, 78–79) showing equigranular microcrystalline dolomite replacement precursor sediment. Photomicrograph taken with a 10× objective.

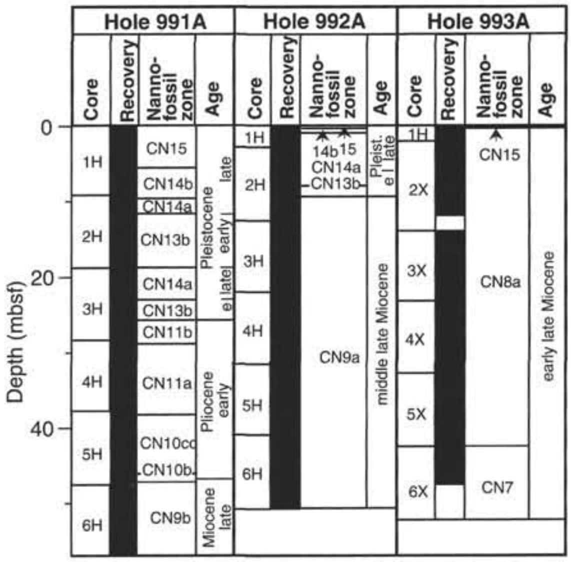

Figure 25. Biostratigraphic summaries for Sites 991, 992, and 993.

Pleistocene may have been removed downslope by repeated slumping at Site 992. This may explain the greater range in ages and possible multiple events exhibited by the mass-transport deposits in Hole 991A, which is on the flank of the diapir at a location that is more likely to accumulate sediments from repeated failures at the upslope locations near the diapir crest. An alternative explanation for the occurrence of mass-transport deposits at Sites 991 and 992 is that they are actually part of the larger Cape Fear Slide complex and were emplaced when downslope movement of the Cape Fear Slide removed some sediments overlying the diapir and left these deposits behind on the diapir's flank and crest.

The basal section (Unit II) in Hole 992A appears to record continuous hemipelagic sedimentation during middle late Miocene times (see "Biostratigraphy" section, this chapter) and probably represents undisturbed, in-place sediments uplifted on the diapir. Seismic data suggest that Hole 993A was drilled in a zone of sediment removal (i.e., a slump/slide scarp) on a very steep portion of the seaward flank of the diapir (Fig. 5). The entire sedimentary section (Subunit IB) from 0.06 mbsf to the base of Hole 993A appears to represent in-place, undisturbed hemipelagic sediments deposited during the early late Miocene. These sediments are similar to, although slightly older than, the middle upper Miocene interval recovered in Unit II in Hole 992A. Apparently all sediments deposited at Site 993 between the early late Miocene and the latest Quaternary have been removed by mass-wasting processes, either as a result of localized sediment failure on the diapir or by downslope movement of the Cape Fear Slide.

Thin intervals (4–6 cm thick) of brownish calcareous sediment form Subunit IA at the top of Holes 991A and 993A (a similar thin, brownish interval occurs at the top of Hole 992A, also Subunit IA, but it appears to be deformed and displaced). These brownish sediment intervals appear similar to other brownish calcareous clay to ooze intervals of approximately Holocene age that previously were cored at the seafloor-sediment interface in this region (e.g., Heezen et al., 1966) and at many other locations in the Atlantic. At most of these

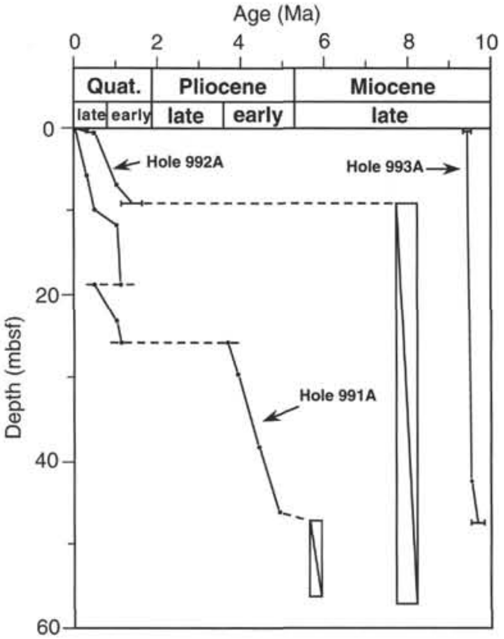

Figure 26. Age-depth relationships of biostratigraphic markers of calcareous nannofossils, Holes 991A, 992A, and 993A. Horizontal error bars show age uncertainties, and boxes indicate combinations of minimum stratigraphic interval and age uncertainties.

locations, this brownish oxidized zone records the decrease in terrigenous sediment supply to the Atlantic in response to a Holocene sea-level rise (see Damuth, 1977, and references therein).

BIOSTRATIGRAPHY

At the three sites drilled on the Cape Fear Diapir, discontinuous sequences of late Neogene and Quaternary age were recovered. Nannofossils are generally abundant, and reasonably detailed age identification was possible at all three sites. Tentative zonal identifications and sediment accumulation rates estimated solely from the nannofossil biostratigraphy are summarized in Figures 25 and 26.

Hole 991A

The section recovered from this hole ranges in age from late Pleistocene to late Miocene. Calcareous nannofossils are generally abundant in the Pleistocene and Pliocene sequences but are rare and even absent in some upper Miocene materials. Preservation is good in the upper Pleistocene sediments and generally moderate in the remainder of the section. Slight and moderate etchings are evident in the lower Pliocene and upper Miocene flora, respectively. Overgrowths are not observed on most nannofossil samples except the lower Pliocene samples from Core 164-991A-5H, which are weakly overgrown.

Ascidian spicules of family Didemnidae, which lives in near-shore waters shallower than ~20 m, are found in most samples throughout the recovered cores, indicating downslope reworking of inner-shelf deposits. Reworked nannofossils are rather rare in most samples. Eocene and Cretaceous forms constitute the majority of redeposited nannofossils.

Pleistocene

The upper four sections of Core 164-991A-1H contain *Emiliania huxleyi,* which indicates Zone CN15. Besides the dominant to common *E. huxleyi,* various species and forms of the genus *Gephyrocapsa,* including *Gephyrocapsa oceanica* (s. str.), are abundant components of the flora. The last occurrence (LO) of *Pseudoemiliania lacunosa* is within the upper part of Section 164-991A-2H-1; therefore, the lower five sections of Core 164-991A-1H belong to Subzone CN14b. Small forms of *Gephyrocapsa* are dominant in most of the samples examined for these sections. Samples 164-991A-2H-1, 74–75 cm, and 2H-2, 80–81 cm, contain nannoflora of Subzone CN14a, in which *Reticulofenestra minuta* (= *Reticulofenestra parvula*) is the most abundant species. Because *Reticulofenestra asanoi* is not present in these samples and the interval assigned to Subzone CN14a (duration: 0.48–0.56 m.y.) is much shorter than that of Subzone CN14b (duration: 0.19 m.y.), there is a strong possibility of a short gap within the upper three sections of Core 164-991A-2H (see Fig. 11, "Explanatory Notes" chapter, this volume, and Fig. 25, this chapter).

Samples 164-991A-2H-2, 134–135 cm, through 2H-CC can be correlated to the upper part of Subzone CN13b. *R. asanoi* is present, and *Helicosphaera sellii* is absent in this flora. Thus, the lower Pleistocene sequence recovered in this hole is younger than 1.17 Ma (the earliest first occurrence [FO] of *R. asanoi*).

Nannoflora of Subzones CN14a to upper CN13b recur in the upper to middle sections of Core 164-991A-3H (Fig. 25). Because the thickness of Subzone CN13b is much shorter in Core 164-991A-3H than that observed in overlying Core 2H, repeated coring is unlikely to be the cause of the repetition of the sequence. Therefore, a minor slide is suspected.

Pliocene

Sections 164-991A-3H-5 through 5H-6 yield lower Pliocene nannoflora that indicate Zones CN11 and CN10. Thus, a sedimentary gap with a duration of more than 2.5 m.y., corresponding to Subzone CN13a and Zone CN12, is suspected between Samples 164-991A-3H-5, 75–76 cm, and 3H-5, 143–144 cm (Fig. 8, "Site 994" chapter, this volume). Because of the presence of *Discoaster tamalis,* Samples 164-991A-3H-5, 143–144 cm, through 4H-1, 6–7 cm, are assigned to Subzone CN11b. *R. minuta, Reticulofenestra pseudoumbilica,* and small *Gephyrocapsa* are abundant, and *Coccolithus pelagicus* and *Discoaster pentaradiatus* are common in these samples. Typical specimens of *P. lacunosa* also were observed in this flora. Samples 164-991A-4H-1, 125–126 cm, through 4H-CC belong to Subzone CN11a. *R. minuta* dominates the flora, and *C. pelagicus, D. pentaradiatus,* and *Sphenolithus abies* are major species in this flora. Typical *P. lacunosa* is absent, whereas the FO of specimens conferrable to this taxon was recognized in the lower part of this subzone. Ceratoliths are generally rare, and besides *Ceratolithus separatus* the other ceratoliths are not identifiable at the species level.

Rare *Amaurolithus delicatus* and *Ceratolithus rugosus* are in Sample 164-991A-5H-1, 75–76 cm, indicating that the interval between this sample and Sample 164-991A-5H-6, 30–31 cm, is assignable to Subzones CN10d–CN10c. The flora is much the same as in Subzone CN11a, except for the presence of *Amaurolithus* spp. and absence of *P.* cf. *lacunosa.*

Because of the moderately advanced dissolution of nannofossils, especially for placoliths, relative abundances of discoasters and ceratoliths in Sample 164-991A-5H-6, 145–146 cm, are higher than in adjacent samples. Ceratoliths observed in this sample are *A. delicatus, Amaurolithus primus, Amaurolithus tricorniculatus, Ceratolithus acutus,* and *Ceratolithus armatus.* The presence of *C. acutus* and absence of *C. rugosus* indicate that this sample belongs to Subzone CN10b. Sample 164-991A-5H-CC was only 1 m lower and contains nannoflora of Subzone CN9b. This suggests that there is a short gap representing the uppermost Miocene at this site.

Miocene

Samples 164-991A-5H-CC through 6H-CC contain upper upper Miocene nannoflora. In Sample 164-991A-5H-CC common *Dis-*

coaster quinqueramus, whose presence defines Zone CN9, were observed. Rare *A. tricorniculatus* also occurs in this sample, restricting the zonal identification to Subzone CN9b. Although Samples 164-991A-6H-2, 80–81 cm, through 6H-4, 80–81 cm, are barren of nannofossils, Samples 164-991A-6H-5, 75–76 cm, through 6H-CC contain few to abundant nannoflora in which *Discoaster berggrenii* and *D. quinqueramus* are common. Ceratoliths are not common in these samples, but rare *A. tricorniculatus,* a possible descendant of *A. delicatus,* exists in Sample 164-991A-6H-CC. Because *Amaurolithus amplificus* does not occur in this sample, the age of the oldest sediment recovered from Hole 991A is constrained from 5.6 Ma (LO of *D. quinqueramus*) to 5.9 Ma (LO of *A. amplificus*).

Hole 992A

Pleistocene and upper Miocene sequences were recovered from this hole. Preservation of nannofossils is good in the Pleistocene sediments and moderate in the Miocene sequence. Slight to moderate degrees of etching are evident in the Miocene flora, but overgrowths are entirely absent, except in Section 164-992A-5H-3, where discoasters show slight overgrowth. Although not in large numbers, ascidian spicules are consistently present throughout the recovered sequence.

Pleistocene

Sample 164-992A-1H-1, 0–1 cm, contains the uppermost Quaternary nannoflora of Zone CN15. In this sample, however, medium *Gephyrocapsa* spp. dominates the flora, and *E. huxleyi* is common, indicating an age of 0.085 Ma (FO of *E. huxleyi* acme) to 0.27 Ma (FO of *E. huxleyi*). Thus, we did not recover Holocene sediment from this hole. Sample 164-992A-1H-1, 75–76 cm, yields nannoflora assignable to Subzone CN14b. Various forms and species of *Gephyrocapsa* and *R. minuta* are abundant components of the flora.

Sample 164-992A-1H-1, 140–141 cm, contains common *P. lacunosa,* whose LO defines the top of Subzone CN14a. Because the thickness of Zone CN15 and Subzone CN14b is significantly thinner than the underlying Subzone CN14a (Fig. 25), there is a strong possibility of a short sedimentary gap within Section 164-992A-1H-1, corresponding to parts of Zone CN15 and Subzone CN14b. Samples 164-992A-1H-1, 140–141 cm, through 2H-3, 74–75 cm, were assigned to Subzone CN14a. Small forms of *Gephyrocapsa, R. minuta* (another small taxon), and *P. lacunosa* are abundant, and *Helicosphaera carteri* and *Syracospahera* spp. are common members of this flora.

Sample 164-992A-2H-4, 2–3 cm, yields dominant small *Gephyrocapsa* but no medium to large forms of *Gephyrocapsa,* and so is assignable to the upper part of Subzone CN13b. The next sample, 164-992A-2H-5, 2–3 cm, contains early Pleistocene forms of *Gephyrocapsa* and rare *H. sellii* but no *Calcidiscus macintyrei,* which indicates the middle part of Subzone CN13b.

Miocene

A significant gap spanning from lower Pleistocene to uppermost Miocene was identified at 9.21 mbsf in Section 164-992A-2H-5, where an unconformity and clear color change were observed. The sections below this level to the bottom of hole were assigned to middle upper Miocene Subzone CN9a. Because rare to few specimens of *Minylitha convallis* occur with common *D. berggrenii* and *D. quinqueramus* throughout this interval, these sections are assignable to the lower half of Subzone CN9a. Thus, the bottom age of this hole is confined between 7.7 Ma (LO of *M. convallis*) and 8.2 Ma (FO of *D. quinqueramus*).

Hole 993A

Except for the top 6 cm of the sediment recovered in Section 164-993A-1H, sediments throughout this hole contain abundant nannofossils of early late Miocene age. Preservation is moderate because of weak to moderate dissolution, and no overgrown nannofossils were observed. The top 6 cm of light brown sediment overlying the olive gray Miocene sediment contains ~10%–20% of the latest Quaternary specimens mixed with 80%–90% of reworked Neogene nannofossils. A few Cretaceous forms also are present in this sediment.

Samples 164-993A-1H-1, 75–76 cm, through 5X-CC contain *Discoaster bollii* and *Discoaster neohamatus. Discoaster hamatus* is not present, except for rare reworked specimens in some samples. This assemblage is assignable to the lower part of Subzone CN8a. The major species observed in this flora are *C. pelagicus, Discoaster braarudii, D. neohamatus, Discoaster variabilis, H. carteri, Neosphaera* cf. *coccolithomorpha, S. abies,* and several species of genus *Reticulofenestra. Florisphaera profunda* is still common in this assemblage and a small placolith tentatively identified as *Umbilicosphaera* sp. A is fairly common in most samples.

Samples 164-993A-6X-1, 29–30 cm, through 6X-CC yield occasional specimens of *D. hamatus,* whose total range defines the lower upper Miocene Zone CN7. Because *Minylitha convallis* is common in Sample 164-993A-6H-CC, the bottom age of this core is constrained between 9.5 Ma (LO of *D. hamatus*) and 9.8 Ma (FO of *M. convallis*).

Sedimentation Rate

The sedimentation rate for the Quaternary sequence from Hole 991A varies from 4 to 21 m/m.y., with an average value of 17 m/m.y. Because there appear to be sedimentary gaps as well as repeated sequences caused by slumping within the Pleistocene sequence, this is not a reliable value. Below the gap spanning from the lower Pleistocene to the upper Pliocene, the sedimentation rate for the lower Pliocene is 16 m/m.y.

The average sedimentation rate for the upper Quaternary sequence at Hole 992A is 7 m/m.y., which is significantly lower than the value at Hole 991A (17 m/m.y.). Because these sites are very close to each other, sedimentation rates should be similar between these two sites. The difference of calculated sedimentation rate, therefore, is due to the difference in the amount of sediments lost by slumping. The minimum rate for the middle upper Miocene of Hole 992A is 96 m/m.y.

Except for the 6 cm of Holocene or uppermost Pleistocene sediment recovered, the uppermost Cenozoic sediment, representing the last 9 m.y., was lost at Hole 993A. The sedimentation rate for the lower upper Miocene sequence recovered from this hole is calculated to be at least 210 m/m.y.

PALEOMAGNETISM

Magnetostratigraphy

None of the magnetostratigraphy could be interpreted with confidence at Sites 991, 992, or 993. Remanence before demagnetization ("natural remanent magnetization") is generally less than 5 mA/m (Fig. 27). With the exception of Core 164-991A-1H, NRM inclination is generally very steeply downward, mostly greater than the expected geocentric axial dipole inclination for this latitude ($\mathrm{Inc}_{\mathrm{GAD}}$ = 51°). Core orientation with the Tensor tool allowed declinations from the third core in Holes 991A and 992A to be referred to geographic coordinates. NRM declinations, however, were scattered and ap-

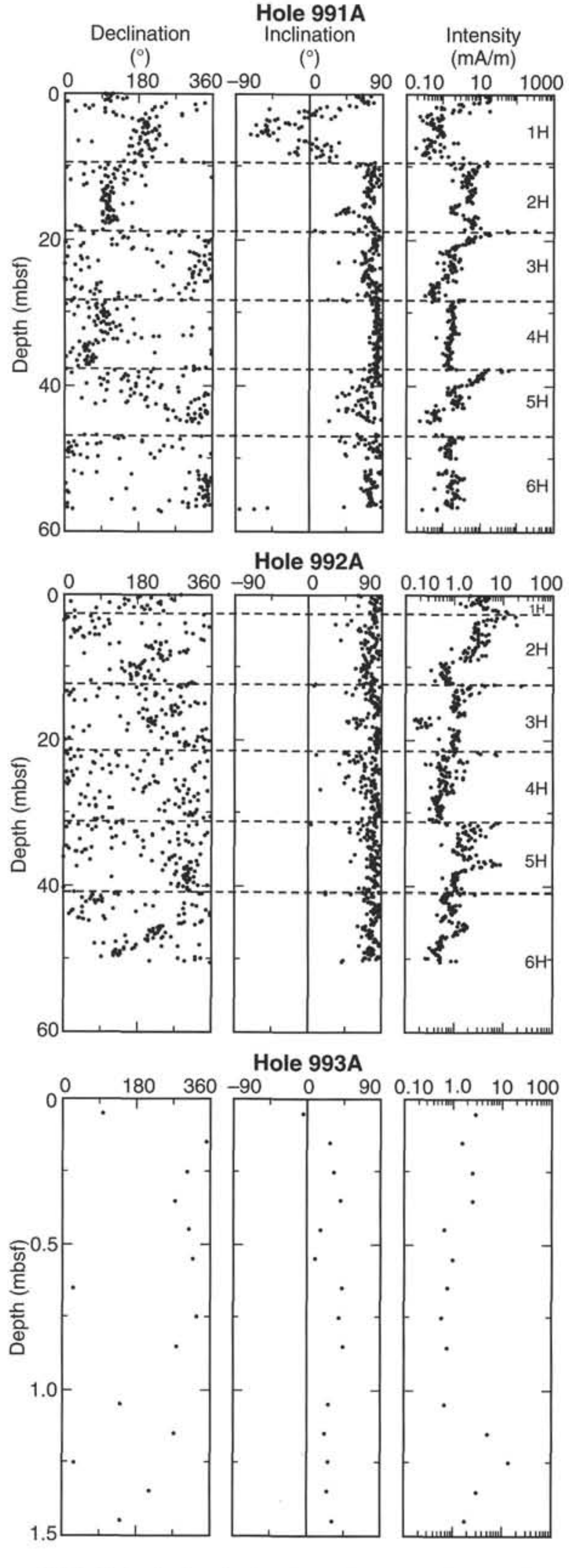

Figure 27. NRM declination, inclination, and intensity. Cores are indicated, with dashed lines marking breaks between cores. Cores 1H and 2H in each hole are unoriented; other cores were oriented with the Tensor tool. Note: Measurements for Hole 993A were made on Core 164-993A-1H only.

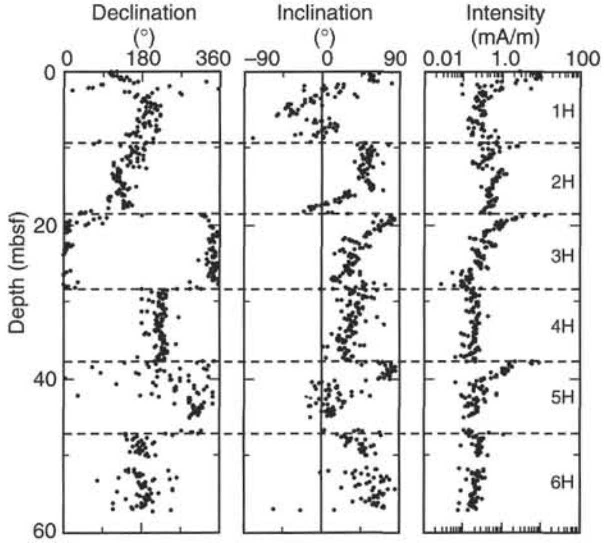

Figure 28. Declination, inclination, and intensity after 25-mT demagnetization for Hole 991A. Core orientation as for Figure 27.

peared to change suddenly at the breaks between successive cores. On the basis of observations from numerous previous ODP legs (e.g., Tauxe et al., 1989; Hall and Sager, 1990; Hounslow et al., 1990; Shipboard Scientific Party, 1992), we interpret the high inclinations and the breaks in the NRM declination record as the result of the acquisition of a "core-barrel overprint" during core recovery.

Routine pass-through AF demagnetization at 10 and 25 mT did not improve resolution of the depositional remanence (Fig. 28). The demagnetized declination record for the oriented cores in Holes 991A and 992A shows distinct breaks between cores after orientation has been conducted. Unoriented demagnetized declinations are aligned along 180° for most of the record in all three holes (Fig. 29), indicating either that the remanence remaining at 25-mT demagnetization is dominated by an overprint with a consistent orientation relative to the core barrel or that some aspect of the measurement process on the cryogenic magnetometer biases very weakly magnetized cores toward the negative x-axis of the magnetometer (see "Explanatory Notes" chapter, this volume).

Demagnetization of discrete samples did not significantly clarify the magnetostratigraphic record. Samples from Hole 991A demagnetize along fairly linear paths from 5 to 25 mT (Fig. 30); inclinations over this interval are all positive. Some samples (e.g., Sample 164-991A-3H-5, 58–60 cm) show evidence of a change in direction of the demagnetization path above 25 mT, suggesting the presence of an unresolved, possibly primary, magnetization. However, remanence above 30 mT was too weak (<0.1 mA/m) to be measured on either of the two shipboard magnetometers.

Samples from Core 164-992A-1H are more strongly magnetized (NRM = ~3 mA/m) and produce a linear demagnetization path up to 40 mT (Fig. 31). This demagnetization path does not converge on the origin, indicating the presence of an unresolved component. Beyond 40 mT, continued AF demagnetization in the GSD-1 demagnetizer induced a severe anhysteretic remanence in these two samples that was not seen to the same extent in other samples from Hole 991A or from Hole 992A.

Whole-Core Magnetic Susceptibility

Magnetic susceptibility measured on the MST for Holes 991A and 992A exceeds 10×10^{-5} (SI, volume normalized) for a short interval near the top of each hole (Fig. 32). In Hole 991A this interval

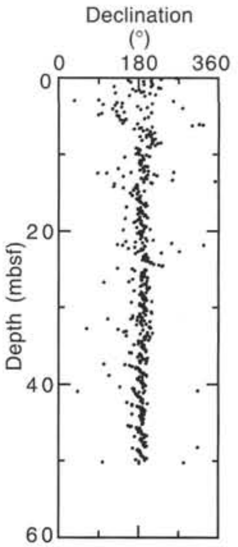

Figure 29. Unoriented declination data after 25-mT demagnetization for Hole 992A.

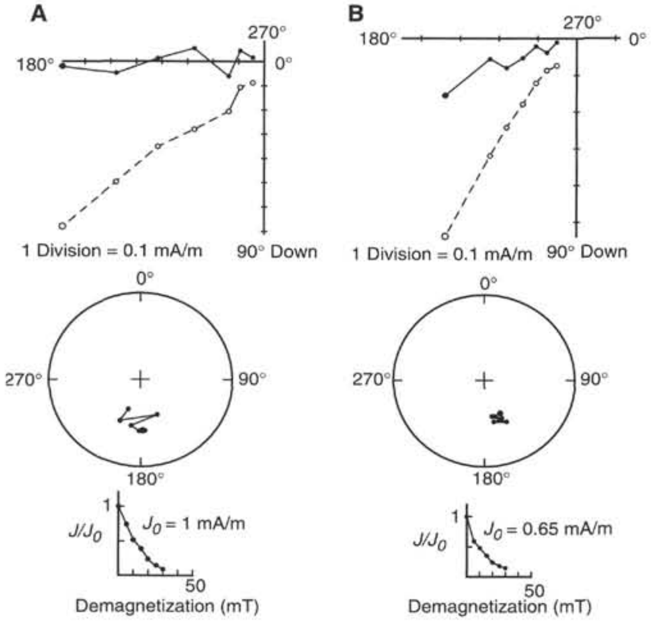

Figure 30. Zijderveld, stereo, and intensity demagnetization plots for (**A**) Sample 164-991A-1H-5, 39–41 cm (6.40 mbsf), and (**B**) Sample 164-991A-3H-5, 58–60 cm (25.19 mbsf). Demagnetization steps increase in 5-mT steps to 30 mT. Zijderveld plot: solid circles = projection on the horizontal plane; open circles = projection on the vertical plane. Stereo plot: solid circles = the lower hemisphere. Intensity plot shows demagnetized intensity normalized to NRM intensity (J_0). Declination is with respect to core coordinates.

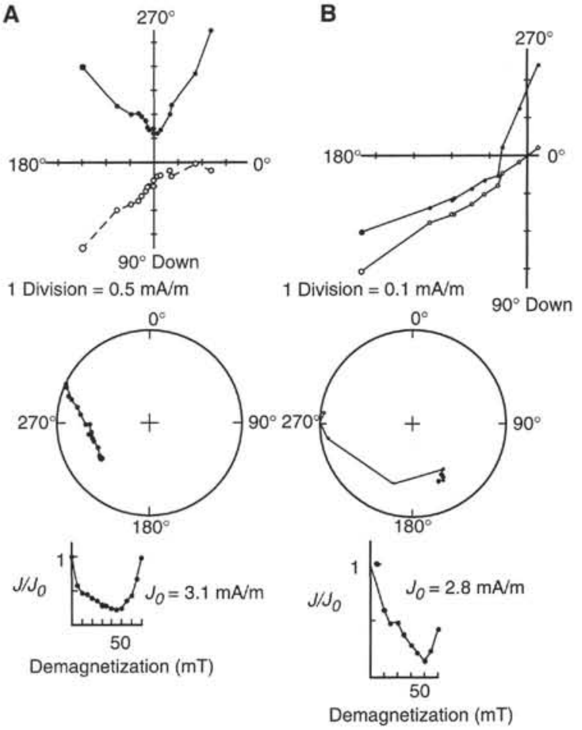

Figure 31. Demagnetization plots for (**A**) Sample 164-992A-1H-1, 39–41 cm (0.40 mbsf), and (**B**) Sample 164-992A-1H-2, 39–41 cm (1.90 mbsf). Symbols and orientation are the same as in Figure 30.

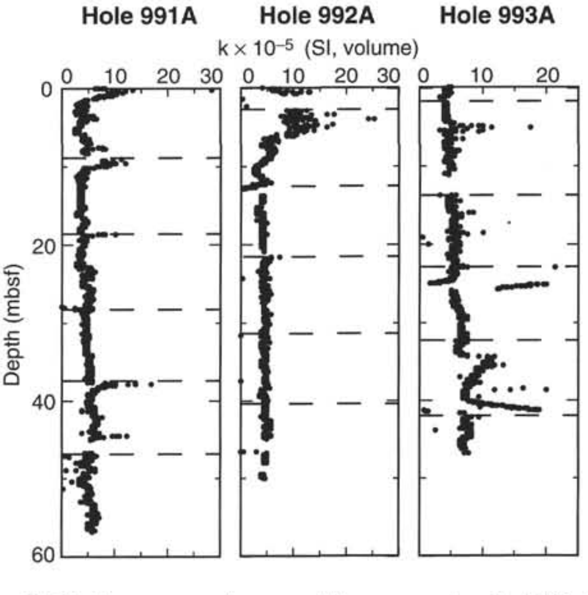

Figure 32. Whole-core magnetic susceptibility measured on the MST after correction for core volume. Dashed lines = core breaks in each hole.

extends to ~1.5 mbsf. Below this depth, susceptibility declines suddenly to settle at a background level of ~3–4 × 10^{-5}, which then slowly increases downhole to ~5–6 × 10^{-5} at the total depth of 56.6 mbsf. Intervals extending for less than 1 m from the top of Cores 164-991A-3H and 5H show local peaks in susceptibility; these may result from rust contamination from the pipe. A similar interval of ~1 m from the top of Core 164-991A-2H may also result from rust contamination, but this is less clear. In Hole 992A an interval of susceptibility exceeding 10 × 10^{-5} extends downhole to ~7 mbsf. From ~7 mbsf downward to the base of Core 164-992A-2H at 12.3 mbsf, susceptibility initially rises (to a maximum of 7 × 10^{-5}), then falls (to a minimum of 3 × 10^{-5}), then rises again. This interval corresponds to a ferroan dolomite horizon. Ferroan dolomite is paramagnetic, and the downhole variations in susceptibility over this interval may reflect changes in the iron content of the dolomite. Below 14 mbsf, susceptibility in Hole 992A also settles into a constant background level of ~3–4 × 10^{-5}, which rises a little less sharply with depth than in Hole 991A, to a maximum of 4–5 × 10^{-5} at 40–50 mbsf.

No initial interval of elevated susceptibility is present in Hole 993A. Instead, the background value of susceptibility rises from ~4 × 10^{-5} near the seafloor to ~7 × 10^{-5} near the bottom of the hole. Superimposed on this trend is a series of susceptibility peaks that do not correspond to core tops. A peak at ~5.5 mbsf can be correlated with a 30-cm-thick dolomite nodule. Although disseminated carbonates are described throughout this hole, other susceptibility peaks do not correspond to any specific lithologic features and may represent some contamination in these heavily biscuited XCB cores.

Rock Magnetism

The intervals of elevated susceptibility at the tops of Holes 991A and 992A correspond to lithostratigraphic Unit I in each hole. Other rock-magnetic parameters also indicate a significant change between Units I and II.

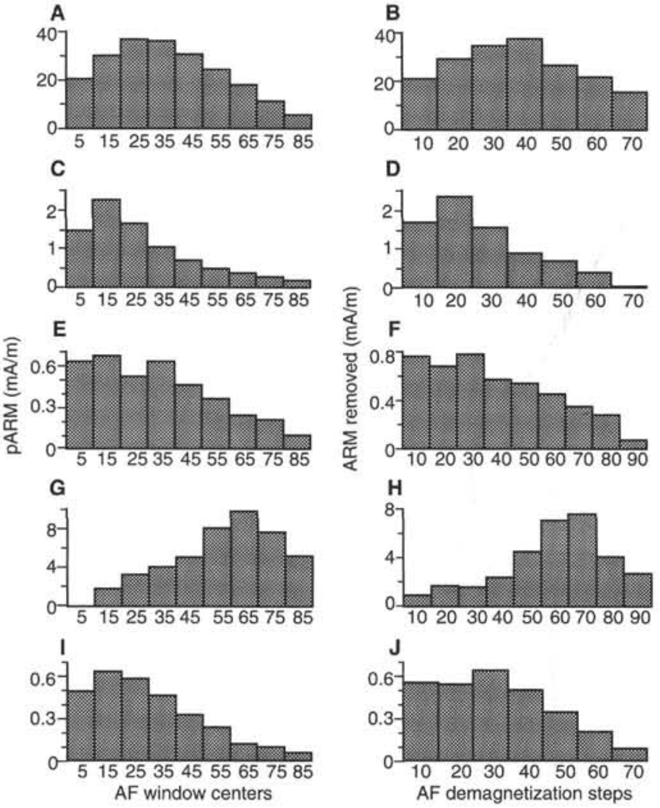

Figure 33. Coercivity spectra illustrated by acquisition of (**A**) pARM and (**B**) dARM of Sample 164-991A-1H-1, 39–41 cm (0.40 mbsf); (**C**) pARM and (**D**) dARM of Sample 164-991A-1H-3, 39–41 cm (3.40 mbsf); (**E**) pARM and (**F**) dARM of Sample 164-991A-6H-5, 59–61 cm (53.70 mbsf); (**G**) pARM and (**H**) dARM of Sample 164-992A-1H-2, 39–41 cm (1.90 mbsf); and (**I**) pARM and (**J**) dARM of Sample 164-992A-2H-6, 39–41 cm (10.70 mbsf). The pARM histograms = centers of AF windows, each 10 mT wide. The dARM histograms = ARM removed between the previous demagnetization step and the step indicated.

Anhysteretic Remanence

Coercivity spectra were investigated through the acquisition of pARM over a series of 10-mT-wide intervals and AF demagnetization of total ARM (dARM) acquired at 70 mT (or, in some cases, 90 mT).

Sample 164-991A-1H-1, 39–41 cm, from within lithostratigraphic Unit I in Hole 991A, shows a simple pARM acquisition spectrum (Fig. 33A) with a broad, single peak centered at 30 mT. A substantial proportion (9.6%) of the total ARM at 90 mT was acquired in the first step (from 0 to 10 mT). Demagnetization of 70-mT ARM of this sample presents a very broad and symmetric spectrum centered at 40 mT (Fig. 33B). Both analyses suggest the presence of one dominant magnetic phase, with a broad distribution of grain sizes. Coercivities in the 30–40 mT range are typical of pseudo-single-domain (PSD) magnetite (Thompson and Oldfield, 1986), and the assemblage may be interpreted as a broad mix of PSD and SD magnetite, with either MD magnetite, or possibly a second magnetic phase.

Sample 164-991A-1H-3, 39–41 cm, taken at 3.4 mbsf, just below the base of Unit I in Hole 991A, has a markedly different pARM spectrum (Fig. 33C). Coercivity is left skewed, with a narrow peak at the 15-mT center, and a broad tail to higher coercivities. A much greater proportion—25%—of the total ARM is acquired in the first 10-mT window. Demagnetization of ARM is similarly left skewed in this sample (Fig. 33D), with a narrow peak at 20 mT. Both plots suggest a greatly diminished proportion of high-coercivity (i.e., SD and PSD) magnetite, relative to larger MD grains. Single-domain magnetite grains typically lie in the range from 0.03 to 1 µm (Dunlop, 1973; Butler and Banerjee, 1975), and these grade through PSD to MD grains at ~10 µm. The shift to a larger grain-size distribution in this sample is accompanied by the decrease in susceptibility from Unit I to Unit II, suggesting that the change in grain-size distribution results from the removal of fine-grained magnetite. Similar dissolution of fine magnetite grain sizes, as part of a diagenetic sequence of progressive reduction steps involving initial authigenic production of magnetite, dissolution of magnetite and replacement by iron monosulfides, conversion of monosulfides to magnetic iron sulfides (greigite and/or pyrrhotite), and final conversion to pyrite, has been well documented in anoxic sediment (e.g., Karlin, 1990; Leslie et al., 1990; Canfield and Berner, 1987).

Sample 164-991A-6H-5, 59–61 cm, located at 53.7 mbsf, displays a further step in downhole modification of the coercivity spectrum. Two peaks appear to be present in the pARM acquisition spectrum (Fig. 33E); this is confirmed by the presence of similar twin peaks in the dARM spectrum (Fig. 33F). This bimodal coercivity spectrum presumably represents two populations of magnetic carriers—either magnetite and another phase or, possibly, two distinct grain-size distributions of magnetite.

Samples from Hole 992A represent part of the same sequence of diagenetic changes in magnetic grain size and mineralogy seen in Hole 991A. Sample 164-992A-1H-2, 39–41 cm, from Unit I in this hole, has strongly right-skewed pARM and dARM coercivity spectra, with peaks at 65 and 70 mT, respectively (Fig. 33G, H). Single-domain (or SD with PSD) magnetite is likely to dominate the magnetic mineralogy in this sample. The tendency of samples from Unit I in this hole to acquire large unintentional ARMs during routine AF demagnetization (see Fig. 31) may also reflect this mineralogy. Sample 164-992A-2H-6, 39–41 cm, was taken at 10.7 mbsf, near the top of Unit II in this hole (Figs. 33I, J). This sample does not display behavior of the type shown near the top of Unit II in Hole 991A, where a single population of magnetite, with a reduced proportion of SD grains, is indicated. Instead, dARM of this sample shows a weakly developed bimodal spectrum similar to, although less well defined than, the dARM spectrum seen near the bottom of Hole 991A. This bimodal distribution is not directly visible in the pARM spectrum of this sample, although it is reflected by the broad peak at 15–25 mT.

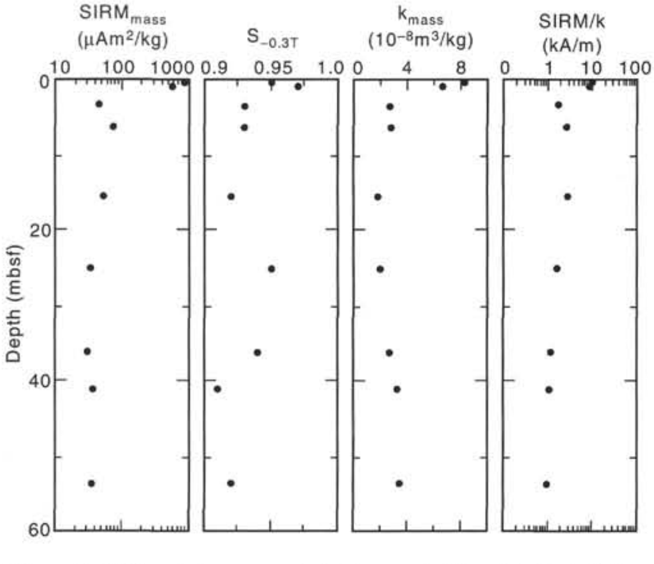

Figure 34. IRM and discrete sample bulk susceptibility plots, Hole 991A.

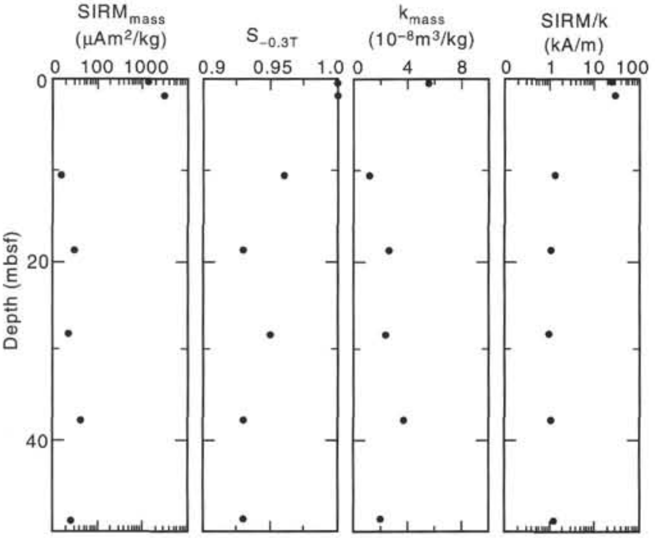

Figure 35. IRM and discrete sample bulk susceptibility plots, Hole 992A.

Again, we interpret the dARM spectrum of this sample to indicate two populations of magnetic carriers, as was the case in the lower part of Unit II in Hole 991A.

Isothermal Remanence

Acquisition of IRM was assessed by imparting SIRM at 1.2 T to the z-axis (downcore) of discrete samples, by measuring this SIRM, and then by imparting an IRM at 300 mT in the −z direction. SIRM was normalized for sample mass, as were the susceptibility measurements for the discrete samples. The $S_{-0.3T}$ (see "Explanatory Notes" chapter, this volume) and SIRM/k ratios, where k = bulk susceptibility, were calculated.

In Hole 991A, $S_{-0.3T}$ is always less than 1, indicating the presence of a magnetic phase other than magnetite (Fig. 34). However, $S_{-0.3T}$ is generally higher in Unit I than in Unit II, indicating that magnetite makes up a greater proportion of the magnetic mineralogy in Unit I than in Unit II. In Unit I in Hole 992A, $S_{-0.3T}$ is greater than 0.995, indicating the almost complete absence of any phase with coercivity higher than magnetite (Fig. 35). In Unit II in Hole 992A, $S_{-0.3T}$ is less than 0.96, indicating an increased proportion of higher coercivity magnetic carriers.

In Hole 991A, SIRM drops by nearly an order of magnitude from Unit I to Unit II. Normalizing SIRM for susceptibility produces an index (SIRM/k) that reflects changes in magnetic mineralogy and/or grain size, rather than the total quantity of ferrimagnetic minerals. Increases in SIRM/k may reflect an increased proportion of SD grains and/or an increase in the amount of the magnetic sulfide greigite (Roberts and Turner, 1993; Musgrave et al., 1995; Housen and Musgrave, 1996), which has been commonly reported in reduced marine sediments. In Hole 991A, SIRM/k follows a path that reflects the changes seen downhole in the ARM behavior. Unit I is characterized by SIRM/k near 1000. At the boundary between Units I and II, SIRM/k initially declines; this correlates with the loss of SD magnetite. SIRM/k then increases again. Although this could reflect renewed growth of SD magnetite, the occurrence of this event below the horizon of significant magnetite dissolution suggests that it results instead from the growth of (probably SD) greigite. Below 20 mbsf in Hole 991A, SIRM/k smoothly decreases. Pyrite was recognized in Core 164-991A-5H, indicating further reduction of greigite to pyrite; loss of greigite explains the decrease downhole in SIRM/k.

Although sparse shipboard sampling limits resolution, the SIRM/k record in Hole 992A appears to lack the interval of increasing SIRM/k seen in the upper part of Unit II in Hole 991A. Instead, Unit II in Hole 992A corresponds to the lower part of Unit II in Hole 991A, with the interval of slowly declining SIRM/k interpreted as resulting from reduction of greigite to pyrite. This matches the ARM behavior seen in Unit II of Hole 992A in which the bimodal signature indicating two magnetic mineralogies is present but relatively suppressed.

Anisotropy of Susceptibility

AMS measurements were limited by the low susceptibility of all samples from all three sites and by rough sea states, which altered the external field environment of the Kappabridge more rapidly than the instrument could respond at sufficiently sensitive measurement levels. The majority of samples from Holes 991A and 992A show susceptibility foliation (F) greater than lineation (L) (see "Explanatory Notes" chapter, this volume), consistent with the observation of overconsolidation in Unit II. However, confidence limits on the measurements were so large (0.02 to 0.1 on each of the three principal susceptibility axes) as to render individual AMS measurements unable to discriminate between oblate and prolate ellipsoids.

Conclusions

The rock-magnetic and susceptibility record in Hole 991A indicates a complete sequence of magnetite-greigite-pyrite reduction steps. The sequence of reduction events in Hole 992A appears to be interrupted at the top of Unit II, consistent with other evidence suggesting removal of the original upper part of Unit II during or before the early Pleistocene. Low susceptibilities characterize the background throughout Hole 993A, consistent with the Miocene age and former burial history at this site. Dissolution of fine-grained (SD) magnetite, and replacement by greigite, has obscured the magneto-

Table 3. Chemistry of water samples from the PCS and FWS, Hole 991B.

Core, interval (cm)	Tool/Sample	pH	Alk (mM)	Sal (g/kg)	Cl^- (mM)	Mg^{2+} (mM)	Ca^{2+} (mM)	SO_4^{2-} (mM)	PO_4^{3-} (µM)	NH_4^+ (µM)	H_4SiO_4 (µM)	K^+ (mM)	Sr^{2+} (µM)
164-991B-													
2P, 40–50	PCS/IW	7.76	23	37.0	644	41	6	1	46	5310	758	13	249
2P, 104	FWS/coil	7.79	4	32.0	522	49	9	25	0	980	43	10	101

Notes: Alk = alkalinity, and Sal = salinity. PCS = pressure core sampler, IW = interstitial water, and FWS = Fisseler Water Sampler.

stratigraphic signal by greatly reducing the NRM intensity and by allowing the acquisition of a severe, high-coercivity core-barrel overprint. AMS, although poorly defined for individual samples, suggests that a foliated (consolidated) fabric dominates Sites 991 and 992.

DOWNHOLE TOOLS AND SAMPLING

Pressure Core Sampler

Run Description

Both PCS runs at Hole 991B were partly successful. Core 164-991B-1P was pressurized at 2550 psi upon reaching the PCS sampling station, but it contained only water. The pressure of 2550 psi is about 67% of that expected for hydrostatic pressure at the coring depth (~2588 mbsl; 3797 psi). Core 164-991B-2P was pressurized at only 63 psi but contained a 1.04-m core of homogenous silty clay.

Geochemical Analyses

The venting of Core 164-991B-1P into the PCS-M2 released 8 mL of liquid and a small amount of gas. The liquid was not sampled for chemical analyses. The manifold design precluded an accurate determination of gas volume. Concentrations of component gases from a single gas sample were below gas chromatography detection limits.

No liquid or gas was released into the manifold upon venting Core 164-991B-2P. However, a portion of this core (40–50 cm) was squeezed for interstitial waters. The chemistry of this sample (Table 3) is similar to that of interstitial waters obtained from sediment recovered at Hole 991A at approximately the same depth (see "Inorganic Geochemistry" section, this chapter).

Fisseler Water Sampler and Chemical Analyses

The FWS successfully recovered 46 mL of water. However, chemical analyses indicate that the water sample is significantly different in composition from interstitial waters recovered at similar depth (51 mbsf) at Hole 991A (see "Inorganic Geochemistry" section, this chapter).

The chemistry of the water collected by the Fisseler tool may provide some insight as to the source of contamination. Concentrations of Cl^-, SO_4^{2-}, Ca^{2+}, and Mg^{2+} (Table 3) can be explained by a mixture of ~90% seawater and 10% distilled (original) water. This observation, in conjunction with sediment on the filter, suggests that seawater in the borehole entered the tool.

ORGANIC GEOCHEMISTRY

The shipboard organic geochemistry program at Sites 991, 992, and 993 included analyses of volatile hydrocarbons; determinations of inorganic carbon, total nitrogen, total carbon, and total sulfur; and Rock-Eval pyrolysis (for a description of methods, see "Explanatory Notes" chapter, this volume).

Volatile Hydrocarbons

Methane (C_1) concentrations were below 100 µL/kg wet sediment in the uppermost sections at each site. At Site 991, a rapid increase in the C_1 concentration to 29,000 µL/kg occurred at 47.10 mbsf (Fig. 36; Table 4). At Site 993, an increase to 27,500 µL/kg occurred at 27.50 mbsf. Decreasing amounts of C_1 (43,200 and 5,620 µL/kg, respectively) were observed in the lowermost samples of Sites 991 and 993. In contrast to Sites 991 and 993, C_1 concentrations never exceed 100 µL/kg at Site 992.

Detectable levels of ethane (C_2), as much as 55 ppmv, were measured from 13.6 mbsf downward at Hole 991A, from 17.3 mbsf downward at Hole 992A, and for all samples at Hole 993A (Table 4). The highest concentration was 55 ppmv at 37.10 mbsf in Hole 993A.

Gas voids were present in cores below 45 mbsf at Holes 991A and 993A, and three of these voids were sampled with vacutainers. Concentrations of C_1 are 117,100 and 349,700 ppmv at 47.6 and 52.1 mbsf, respectively, in Hole 991A; a value of 747,600 ppmv was determined at 45.7 mbsf in Hole 993A (Table 5). Hydrocarbon gases up to C_6 were measured at 45.7 mbsf in Hole 993A. At Hole 991A, 7200 ppmv of hydrogen sulfide was detected at 52.1 mbsf.

Entire core sections (1.5 m in length) were placed into sealed PVC plastic tubes and monitored for gas flow, temperature, and gas composition. The volumes of gas that evolved from these core sections while they warmed to room temperature are given in Table 6. Also given are the calculated volumes of gas that evolved per liter of pore water in the core sections. The values are corrected for water content percentage using the closest measured value (see "Physical Properties" section, this chapter). Values are minimum estimates of the amounts of gas contained within the sediments in situ because the cores were actively degassing before they were placed in the gas-collection chambers. The volumes of gas recovered from Sites 991 and 993 are much higher than those that were recovered from Site 992. Note that significant amounts of gas were collected only from sections where most of the interstitial sulfate was depleted. Gas compositions of these core sections are reported in Table 7.

Total Organic Carbon, Total Nitrogen, and Rock-Eval Analyses

The TOC concentrations of samples from all sites are between 0.32% and 2.59%. In general, the lowest concentrations were found at Site 991; the highest, at Site 992 (Fig. 37; Table 8). The C/N ratios are near 10 in all samples. Measured hydrogen indices (HI) are between 137 and 427 mg hydrocarbons per gram organic carbon, and T_{max} values are in the range from 416° to 435°C.

Discussion

Hydrocarbon gases in immature sediment are typically of microbial origin and characteristically have methane/ethane ratios of >1000 (Schoell, 1980). However, the uppermost two samples from Holes 991A and 993A, and all samples from Hole 992A have C_1/C_2 ratios less than 100. These data may be affected by analytical uncertainties and/or preferential loss of C_1 by oxidation rather than from a

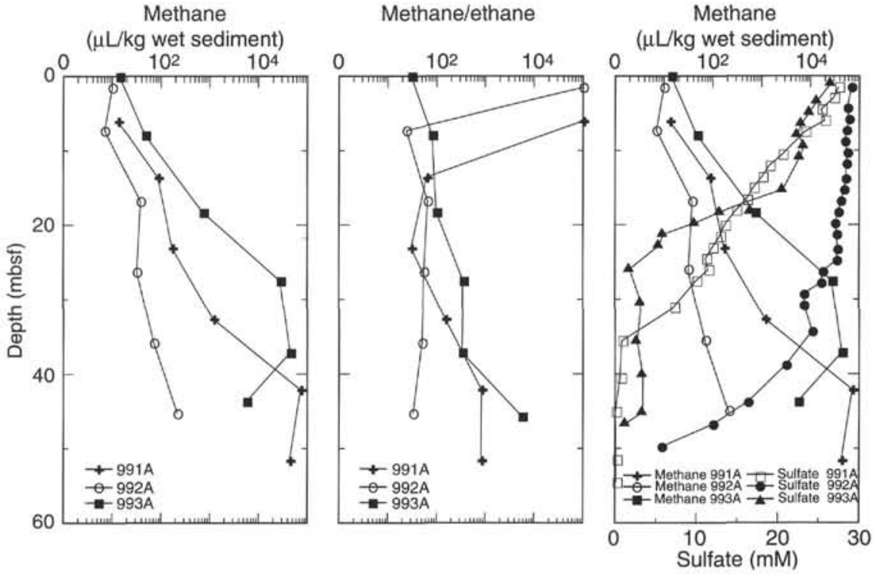

Figure 36. Methane content, methane/ethane ratio, and sulfate/methane content for sediments at Sites 991, 992, and 993.

Table 4. Composition of headpace gas in sediment from Holes 991A, 992A, and 993A.

Core, section	Depth (mbsf)	C_1 (ppmv)	C_2 (ppmv)	C_1/C_2	C_1 (μL/kg wet sediment)
164-991A-					
1H-5	6.00	5		100,000	13
2H-4	13.60	31	0.5	62	86
3H-4	23.10	59	2.0	30	169
4H-4	32.60	432	2.9	149	1,170
5H-4	42.10	29,000	34.8	834	71,800
6H-4	51.60	12,200	14.8	823	43,200
164-992A-					
1H-2	1.50	2		100,000	10
2H-4	7.30	3	0.1	24	7
3H-4	16.80	13	0.2	65	38
4H-4	26.30	11	0.2	55	32
5H-4	35.80	25	0.5	50	71
6H-4	45.30	81	2.5	33	218
164-993A-					
1H-1	0.00	6	0.2	30	14
2X-5	7.90	20	0.2	80	47
3X-4	18.30	174	3.6	98	720
4X-4	27.50	7,330	21.0	349	27,500
5X-4	37.10	18,100	55.0	329	44,000
6X-2	43.70	1,680	0.3	5,600	5,620

Notes: C_1 = methane, and C_2 = ethane. C_1/C_2 = the methane/ethane ratio.

major contribution of thermal gas. Until the isotopic composition of C_1 is measured, an admixture of thermogenic hydrocarbons cannot be substantiated.

The abrupt increases of the C_1 concentrations at 37.6 mbsf at Site 991 and at 23 mbsf at Site 993 correspond to depletion in interstitial sulfate (Fig. 36C). This relationship has been observed at numerous ODP sites (Kvenvolden et al., 1990; Stein et al., 1995). Concentrations of C_1 also increase with depth at Site 992; however, the overall concentration is relatively low and ranges from 7 to 218 μL/kg. The increase in C_1 correlates with decreasing sulfate content of pore water (see "Inorganic Geochemistry" section, this chapter). Therefore, we conclude that at Sites 991 and 993 C_1 is or has been microbially generated below the zone of sulfate reduction. At Site 992, methanogenesis may be limited by the presence of sulfate (Martens and Berner, 1974).

The TOC contents are high for continental rise sediments (as much as 2.59%). The high TOC content is consistent with high sedimentation rates and good preservation of organic matter.

The type of the organic matter has been characterized using organic C/N ratios (Fig. 37) and pyrolysis data (Table 9). The C/N ratios of ~10 in sediment at Sites 991, 992, and 993 indicate a dominance of marine organic material. Average C/N ratios of marine zooplankton and phytoplankton are between 5 and 8, whereas higher land plants have ratios between 20 and 200 (Emerson and Hedges, 1988). Although these values may change during maturation, the low C/N ratios in these immature sediments reflect a marine origin. The HI values measured by Rock-Eval pyrolysis also indicate a marine origin. HI values were calculated using data in Table 8 and the technique of Langford and Blanc-Valleron (1990). Samples from Site 991 have a calculated HI value of 362 mg hydrocarbons/g organic carbon. For Sites 992 and 993, the HI values are 655 and 415 mg hydrocarbons per gram, respectively. T_{max} values are range from 416° to 435°C (mean value is 424°C) for sediment from all three sites, which indicates immaturity or early maturity of the organic matter. The thickness of the eroded part of the overburden cannot be estimated because of a lack of a maturity gradient.

INORGANIC GEOCHEMISTRY

Interstitial-water chemistry varies considerably among Sites 991, 992, and 993 (Table 10) despite the proximity of the sites (within 5 km). The tectonic and hydrologic setting of the Cape Fear Diapir likely influences the interstitial chemistry, although the actual controlling mechanisms are unclear.

Two salient features of the interstitial-water chemistry distinguish these sites from many other pelagic DSDP/ODP sites: (1) significant downhole increases in Cl^- and (2) linear and concave-upward SO_4^{2-} profiles.

Chloride Gradients

Chloride concentrations increase with depth at Sites 991, 992, and 993, reaching maxima of 664, 584, and 642 mM, respectively (Fig. 38). At Sites 991 and 993, the average Cl^- gradient is ~2 mM/m. At Site 992, situated over the crest of the diapir, the average Cl^- gradient

Table 5. Composition of free gas collected in vacutainers from sediments at Sites 991 and 993.

Core, section	Depth (mbsf)	O_2 (ppmv)	N_2 (ppmv)	C_1 (ppmv)	CO_2 (ppmv)	C_2 (ppmv)	H_2S (ppmv)	C_3 (ppmv)	i-C_4 (ppmv)	n-C_4 (ppmv)	i-C_5 (ppmv)	i-C_6 (ppmv)	n-C_6 (ppmv)	C_1/C_2	C_1/C_{2+}
164-991A-															
6H-1	47.60	NA	NA	117,100	NA	89		3.0	NA	NA	NA	NA	NA	1,316	1,273
6H-4	52.10	116,000	487,000	349,700	22,900	275	7,200	12.0	4.0					1,272	1,202
164-993A-															
6X-3	45.70	37,000	158,000	747,600	32,700	1,248		13.3	3.9	0.3	0.1	0.2	0.1	599	590

Notes: Oxygen (O_2) and nitrogen (N_2) concentrations are included as a guide to the amount of air contamination in each sample. C_1 through C_6 = the alkanes: methane, ethane, propane, butane, pentane, and hexane. Iso- and normal configurations of butane, pentane, and hexane are designated with *i*- and *n*- prefixes. C_1/C_2 = the methane/ethane ratio, and C_1/C_{2+} = the ratio of methane/Σ (C_2 through C_6). NA = not analyzed.

Table 6. Volumes of gas collected as whole-core sections warmed to room temperatures within gas-collection chambers, Sites 991, 992, and 993.

Core, section	Depth (mbsf)	Gas collected (mL)	Gas/water ratio (mL/L)
164-991A-			
1H-3	0	0	
2H-3	12	0	0
3H-4	23	0	0
4H-3	32	57	16
5H-3	42	560	181
6H-2	49	220	100
164-992A-			
1H-1	0	0	
2H-3	5	0	0
3H-3	15	0	0
4H-3	24	0	0
5H-3	34	0	0
6H-3	43	0	0
164-993A-			
2X-2	2	0	
3X-3	16	0	0
4X-3	26	290	108
5X-3	35	310	108
6X-3	45	0	0

Notes: Gas/water ratio refers to the amount of gas relative to the calculated amount of pore water within the whole-core section.

is ~0.8 mM/m. Downcore increases in Cl^- display slight upward concavity (Fig. 38).

Sulfate and Alkalinity

The SO_4^{2-} profile at Site 991 is linear in the upper 36 m, whereas the profile at Site 992 is distinctly concave upward (Fig. 38). The SO_4^{2-} profile at Site 993 is much more complex. Sulfate depletion is relatively rapid at Sites 991 and 993, whereas the concentrations of SO_4^{2-} at Site 992 remain close to that of seawater to ~25 mbsf (Fig. 38). The method used to determine SO_4^{2-} (see "Explanatory Notes" chapter, this volume) cannot accurately measure concentrations less than ~1 mM. Thus, values lower than 1 mM are generally interpreted as an absence of SO_4^{2-}. The level of "zero" SO_4^{2-} is reached at ~36 mbsf at Site 991. Concentrations of SO_4^{2-} decrease to a minimum value of 5.8 mM at 49.8 mbsf at Site 992. At Site 993, SO_4^{2-} decreases to a local low of 1.9 mM at 26.0 mbsf and then ranges from 3.5 to 1.4 mM to the bottom of the hole.

The alkalinity of interstitial water at Site 991 increases almost linearly from 3.79 mM in the shallowest sample to 26.88 mM at 35.6 mbsf (Fig. 38). A distinctly concave-upward alkalinity profile occurs at Site 992. Values are less than 5 mM between 1.5 and 21.3 mbsf, and they increase to 20.2 mM between 21.3 and 49.8 mbsf. At Site 993, alkalinity increases to ~28.7 mM at 35.6 mbsf and remains at this level until a decrease to 25.9 mM at the base of the site.

Ammonium

Ammonium concentration profiles are approximately linear at all sites; however, the average NH_4^+ gradient differs significantly. It is 0.1 mM NH_4^+/m at Site 991, 0.4 mM NH_4^+/m at Site 992, and 0.3 mM NH_4^+/m at Site 993 (Fig. 38). The maximum concentrations of NH_4^+ at Sites 991, 992, and 993 are 6.4, 2.1, and 9.7 mM, respectively.

Potassium and Sodium

The K^+ concentrations are nearly constant throughout the sediment column at all sites, whereas the concentrations of Na^+ increase with increasing depth. The K^+/Cl^- ratio in the shallowest samples (0.023 average for the three sites) is significantly higher than that in seawater (0.019; Millero and Sohn, 1992). The concentrations of Na^+ were estimated from charge-balance considerations and are, therefore, subject to a sum of errors in the measurement of all other major ions. This uncertainty is typically ±0.67% of a given individual measurement.

Calcium, Magnesium, and Strontium

At all three sites, Ca^{2+} and Mg^{2+} concentrations decrease with increasing depth. The average Ca^{2+}/Cl^- ratio in all of the shallowest samples is similar to that in seawater, whereas the Mg^{2+}/Cl^- ratio (0.092) is less than that in seawater (0.097; Millero and Sohn, 1992). Concentrations of Sr^{2+} increase with increasing depth at all three sites. The average Sr^{2+}/Cl^- ratio in the shallowest samples (0.00017) is similar to seawater ratios (Millero and Sohn, 1992).

Origin of Chloride Enrichment

Positive Cl^- gradients could be produced by ion exclusion caused by gas hydrate formation (e.g., Hesse and Harrison, 1981; Kastner et al., 1990; Ussler and Paull, 1994), by interaction with brines associated with the core of the diapir, and by dissolution of salt that may form the diapir's core. The observed Cl^- data are consistent with a salt-cored diapir. Maximum reported Cl^- enrichment ascribed to gas hydrate formation is only ~10 mM (Kvenvolden and Kastner, 1990). Chloride enrichment is much higher at the diapir sites, ranging from 30 to 90 mM downhole (Table 10). In evaporitic environments, brines may form through dissolution of salt or can be present as residual water formed by evaporation of seawater. In the case of halite dissolution, the Na^+/Cl^- ratio should increase toward unity when plotted vs. the concentration of Cl^- (Fig. 39). An opposite trend (Na^+/Cl^-

Table 7. Composition of the gas collected from whole 1.5-m sections from Sites 991 and 993.

Core, section	Depth (mbsf)	O_2 (ppmv)	N_2 (ppmv)	C_1 (ppmv)	CO_2 (ppmv)	C_2 (ppmv)	C_3 (ppmv)	i-C_4 (ppmv)	n-C_5 (ppmv)	i-C_6 (ppmv)	C_1/C_2	C_1/C_{2+}
164-991A-												
5H-3	40.60	174,000	726,000	64,000	4,400	51.8	1.7	0.9	0.8	0.3	1,240	1,150
6H-2	48.60	129,000	742,000	100,900	4,300	91.0	1.5	0.7	0.6	0.4	1,110	1,070
164-993A-												
5X-3	35.60	NA	NA	427	1,230			NA	NA	NA		
4X-4	27.50	NA	NA	73	910			NA	NA	NA		

Notes: Oxygen (O_2) and nitrogen (N_2) concentrations are included as a guide to the amount of air contamination in each sample. C_1 through C_6 = the alkanes: methane, ethane, propane, butane, pentane, and hexane. Iso- and normal configurations of butane, pentane, and hexane are designated with *i*- and *n*- prefixes. C_1/C_2 = the methane/ethane ratio, and C_1/C_{2+} = the ratio of methane/Σ (C_2 through C_6). NA = not analyzed.

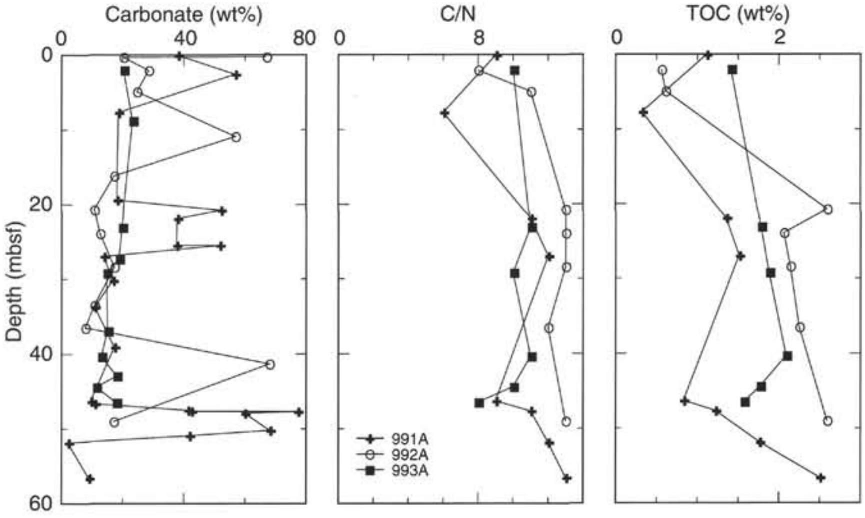

Figure 37. Carbonate content, C/N ratio, and total organic carbon content of sediments from Sites 991, 992, and 993.

ratios decreasing with increasing Cl^- content) should be observed if high-salinity waters are formed by mixing seawater and a residual brine (Brantley et al., 1984). Unfortunately, the errors in these data are too large to confidently distinguish between these models (Fig. 39).

Factors Controlling Sulfate Depletion

Sulfate profiles in deep-sea sediments are usually concave downward, although linear profiles like those observed at Site 991 are not uncommon (e.g., Egeberg and Abdullah, 1990; Borowski et al., in press). Linear SO_4^{2-} profiles can be attributed to extensive SO_4^{2-} depletion in a restricted subsurface interval accompanied by downward SO_4^{2-} diffusion. Shipboard analyses of organic carbon and total nitrogen percentages did not indicate the presence of significant variations or particularly organic-rich sediment at any of the sites (see "Organic Geochemistry" section, this chapter). The linear SO_4^{2-} profile at Site 991 suggests that SO_4^{2-} consumption above 36 mbsf is negligible relative to the rate of SO_4^{2-} depletion at the CH_4/SO_4^{2-} boundary. CH_4 is the probable substrate involved in SO_4^{2-} consumption via anaerobic methane oxidation ($SO_4^{2-} + CH_4 \rightarrow HCO_3^- + HS^- + H_2O$; Reeburgh, 1976). Furthermore, the linear profile implies steady-state, diffusive conditions. For a detailed discussion of linear SO_4^{2-} profiles occurring in the Blake Ridge vicinity, see the "Inorganic Geochemistry" section in the "Site 994" chapter (this volume).

The concave-upward depth profiles of SO_4^{2-} and alkalinity at Site 992 may suggest very slow downward advection of seawater, consistent with significantly shallower gradients in Cl^-, Mg^{2+}, Ca^{2+}, and Sr^{2+} (Fig. 38; Table 10) and suppressed methane levels relative to Sites 991 and 993 (see "Organic Geochemistry" section, this chapter). The rate of flow is not sufficient to overprint chemical signals created by the microbial consumption of organic matter (i.e., consumption of SO_4^{2-}, production of alkalinity, and release of NH_4^+). Downward advection of seawater in sediment above a diapir can be understood by considering the effects of temperature and salinity upon the density of seawater. Although evaporites have higher thermal conductivities, any increased buoyancy of water caused by heating is overwhelmed by increases in salinity over the interval between the salt core and the sediment surface. Alternatively, linear, apparently undisrupted NH_4^+ profiles imply diffusive, steady-state conditions exclusive of any fluid advection. Decreased SO_4^{2-} consumption may reflect lower levels of upward-diffusing CH_4 that fuels SO_4^{2-} depletion at the base of the SO_4^{2-} reduction zone at Site 991.

The complex SO_4^{2-} profile (and perhaps other profiles) at Site 993 (Fig. 38) suggests that interstitial-water conditions are nonsteady state. Coexistence of high levels of CH_4 (Fig. 36) with diminished, but nonzero SO_4^{2-} concentrations at Site 993 also is anomalous. These chemical observations may reflect downward seawater advection, changes in upward CH_4 flux, or a SO_4^{2-} profile re-equilibrating from sediment removal via slumping.

PHYSICAL PROPERTIES

The shipboard physical properties program at Sites 991, 992, and 993 included nondestructive continuous measurements of GRAPE wet bulk density, bulk magnetic susceptibility, *P*-wave velocity, and NGR activity on nearly all sections of recovered cores. More than half of the high-resolution PWL data had to be discarded because only the velocity of the liner was recorded. Index properties, which are presented in Table 11, were measured on samples recovered from split sections. Thermal conductivity data were collected for all APC cores from Sites 992 and 993. Strength was measured at discrete points (one per section to one per core) using the vane shear apparatus

Table 8. Carbonate, carbon, nitrogen, and sulfur contents in sediments from Sites 991, 992, and 993.

Core, section, interval (cm)	Depth (mbsf)	Inorganic carbon (wt%)	$CaCO_3$ (wt%)	Organic carbon (wt%)	Total nitrogen (wt%)	C/N	Total sulfur (wt%)
164-991A-							
1H-1, 5–6	0.05	4.56	38.0	1.11	0.12	9	0.14
1H-2, 108–109	2.58	6.81	56.7	NA	NA	NA	NA
1H-6, 20–21	7.70	2.22	18.5	0.32	0.05	6	0.74
3H-1, 80–81	19.40	2.17	18.1	NA	NA	NA	NA
3H-2, 67–68	20.77	6.24	52.0	NA	NA	NA	NA
3H-3, 29–30	21.89	4.52	37.7	1.35	0.12	11	1.14
3H-5, 89–90	25.49	4.50	37.5	NA	NA	NA	NA
3H-5, 90–91	25.50	6.19	51.6	NA	NA	NA	NA
3H-6, 86–87	26.96	1.65	13.7	1.51	0.13	12	1.29
4H-2, 59–60	30.19	2.00	16.7	NA	NA	NA	NA
4H-4, 112–113	33.72	1.30	10.8	NA	NA	NA	NA
5H-1, 146–147	39.06	2.07	17.2	NA	NA	NA	NA
5H-6, 120–121	46.30	1.14	9.5	0.83	0.10	9	3.85
5H-7, 2–3	46.62	1.30	10.8	NA	NA	NA	NA
6H-1, 40–41	47.50	4.94	41.2	NA	NA	NA	NA
6H-1, 54–55	47.64	5.09	42.4	1.22	0.11	11	1.19
6H-1, 58–59	47.68	9.26	77.1	NA	NA	NA	NA
6H-1, 80–81	47.90	7.18	59.8	NA	NA	NA	NA
6H-3, 10–11	50.20	8.16	68.0	NA	NA	NA	NA
6H-3, 80–81	50.90	5.00	41.7	NA	NA	NA	NA
6H-4, 23–24	51.83	0.25	2.1	1.76	0.15	12	1.60
6H-7, 48–49	56.58	1.07	8.9	2.50	0.19	13	2.11
164-992A-							
1H-1, 26–27	0.26	8.03	66.9	NA	NA	NA	NA
1H-1, 30–31	0.30	2.43	20.2	NA	NA	NA	NA
1H-2, 56–57	2.06	3.41	28.4	0.56	0.07	8	0.50
2H-2, 61–62	4.91	2.95	24.6	0.61	0.06	11	0.37
2H-6, 59–60	10.89	6.82	56.8	NA	NA	NA	NA
3H-3, 84–85	16.14	2.06	17.2	NA	NA	NA	NA
3H-6, 90–91	20.70	1.29	10.7	2.59	0.19	13	2.35
4H-2, 60–61	23.90	1.50	12.5	2.06	0.16	13	1.84
4H-5, 60–61	28.40	2.07	17.2	2.14	0.16	13	1.84
5H-2, 70–71	33.50	1.29	10.7	NA	NA	NA	NA
5H-4, 70–71	36.50	0.92	7.7	2.25	0.19	12	2.15
6H-1, 50–51	41.30	8.15	67.9	NA	NA	NA	NA
6H-6, 70–71	49.00	2.04	17.0	2.59	0.20	13	2.01
164-993A-							
2X-1, 10–11	2.00	2.43	20.2	1.41	0.14	10	2.28
2X-5, 90–91	8.80	2.79	23.2	NA	NA	NA	NA
3X-7, 26–27	23.06	2.36	19.7	1.78	0.16	11	1.85
4X-3, 132–133	27.32	2.24	18.7	NA	NA	NA	NA
4X-5, 20–21	29.20	1.76	14.7	1.88	0.18	10	2.04
5X-3, 132–133	36.92	1.80	15.0	NA	NA	NA	NA
5X-6, 21–22	40.31	1.56	13.0	2.09	0.20	11	1.20
6X-1, 70–71	42.90	2.16	18.0	NA	NA	NA	NA
6X-2, 70–71	44.40	1.36	11.3	1.77	0.18	10	1.11
6X-3, 126–127	46.46	2.14	17.8	1.57	0.19	8	1.34

Note: NA = not analyzed.

and a pocket penetrometer, and *P*-wave velocities were determined at discrete locations using the DSV. Raw data not given in tabular form within this chapter are available on CD-ROM (back pocket).

Hole 991A

The results of physical properties measurements on cores recovered from Hole 991A are shown in Figure 40.

Index Properties

Bulk densities calculated using the wet method (see "Index Properties Measurements" in the "Physical Properties" section of the "Explanatory Notes" chapter, this volume) vary from 1.49 to 1.92 g/cm^3 downhole, with the only significant variations occurring at depths shallower than 4 mbsf and deeper than 44 mbsf. Water contents calculated using the wet and dry methods vary from 28% to 53% and from 39% to 113%, respectively, with values decreasing with depth to 50 mbsf. Porosity (wet method) varies from 77% near the top of the section to 52% at the bottom and follows the same decreasing trend as the water-content data.

Acoustic Velocity

The *P*-wave velocity plot shows the presence of a peak at 12 mbsf, where values increase from 1.50 to 1.56 km/s. Below this level, velocity increases gradually from 1.51 to 1.55 km/s. Where high-quality DSV measurements could be obtained, velocity values generally agree with the data collected by the *P*-wave logger. DSV results imply a sharp drop in seismic velocity to 1.47 km/s, but this pattern is hard to confirm without the high-resolution PWL data.

Undrained Shear Strength

Vane shear measurements show a gradual increase in strength from nearly 0 kPa at the surface to 20 kPa at 10 mbsf. Strength increases markedly to 60 kPa just below 10 mbsf but then increases more slowly to ~100 kPa at 44 mbsf. Pocket penetrometer measurements indicate a sharp increase in strength to >150 kPa at 44 mbsf, with an almost exponential decrease to 80 kPa deeper in the section.

Natural Gamma Radiation

NGR measurements on unsplit sections show a positive peak of more than 20 counts above the average value at 10 mbsf. In the rest of the section, NGR values vary little, although the smallest value recorded (2 counts/s) does coincide with changes in grain density and strength at approximately the same depth.

Physical Properties Units

Two physical properties units are distinguished at Site 991: Unit A (0–44 mbsf) has relatively constant index properties, GRAPE wet bulk density, and undrained shear strength. Most of the variations in physical properties in the uppermost 2–5 m of Hole 991A are near-seafloor effects evident at all three sites (991, 992, and 993). Physical properties Unit A correlates with lithostratigraphic Units I and II. Unit B (44–57.16 mbsf) is distinguished from Unit A by an increase in bulk density and strength and by changing grain densities with depth. Unit B corresponds to lithostratigraphic Unit III, which is described as a relatively undeformed sequence of silty clay and nannofossil-bearing clayey silt with a capping 4-cm-thick layer of carbonate-bearing clay. Increased strength near the top of Unit B may reflect the presence of significant amounts of carbonate at this depth.

Hole 992A

Figure 41 summarizes the physical properties results obtained on sediments recovered from Hole 992A.

Index Properties

GRAPE measurements reveal a significant change in wet bulk density with depth, yielding values as high as 2 g/cm^3 in the uppermost 12 mbsf. Below this depth, wet bulk densities lie in a narrow range from 1.6 to 1.8 g/cm^3 and generally increase as a function of depth. The wet bulk density values obtained from index properties measurements follow the general trend of the GRAPE data below 12 mbsf but are offset from the GRAPE data by 0.2 g/cm^3. Water contents vary from 34% to 48% (wet) and from 53% to 94% (dry) over the length of the hole, but they are relatively constant below 12 mbsf. Wet porosity increases from 60% to 70% in the upper 10 m and is constant (70%) below this depth. Dry grain density varies in a narrow range from 2.52 to 2.76 g/cm^3.

Table 9. Rock-Eval analyses of sediments from Sites 991, 992, and 993.

Core, section, interval (cm)	Depth (mbsf)	T_{max}	S_1	S_2	S_3	PI	HI	OI
164-991A-								
1H-1, 5–6	0.05	424	0.80	2.19	3.56	0.27	197	320
3H-3, 29–30	21.89	416	0.73	2.71	2.96	0.21	200	219
3H-6, 86–87	26.96	421	0.73	3.02	2.16	0.20	200	143
6H-1, 40–41	47.64	427	0.36	2.46	1.26	0.13	201	103
6H-4, 23–24	51.83	435	0.67	7.52	1.12	0.08	427	63
6H-7, 48–49	56.58	429	0.55	6.93	1.91	0.07	277	76
164-992A-								
3H-6, 90–91	20.70	416	1.01	7.80	2.33	0.11	301	89
4H-2, 60–61	23.90	428	0.40	5.17	1.99	0.07	250	96
4H-5, 60–61	28.40	420	0.40	5.05	2.34	0.07	235	109
5H-4, 70–71	36.50	415	0.96	5.51	2.22	0.15	244	98
6H-6, 70–71	49.00	420	0.94	8.77	2.38	0.10	338	91
164-993A-								
2X-1, 10–11	2.00	424	0.20	1.94	2.12	0.09	137	150
3X-7, 26–27	23.06	427	0.29	3.12	2.26	0.09	175	126
5X-6, 70–71	40.31	429	0.36	4.49	2.21	0.07	214	105
6X-1, 21–22	42.90	430	0.43	4.81	2.04	0.08	255	108
6X-2, 70–71	44.40	420	0.58	3.73	2.12	0.13	210	119

Notes: T_{max} = temperature (°C) at which the maximum amount of hydrocarbons are generated from the kerogen during pyrolysis; S_1 = quantity of free hydrocarbons in the rock samples, in mg/g rock; S_2 = quantity of hydrocarbons produced by kerogen cracking, in mg/g rock; S_3 = quantity of organic CO_2 produced during pyrolysis of the rock, in mg/g rock; PI = production index, calculated as S_1/S_1+S_2; HI = hydrogen index, calculated as S_2/TOC; and OI = oxygen index, calculated as S_3/TOC.

Table 10. Interstitial-water data for Sites 991, 992, and 993.

Core, section, interval (cm)	Depth (mbsf)	pH	Alk (mM)	Sal (g/kg)	Cl^- (mM)	Mg^{2+} (mM)	Ca^{2+} (mM)	SO_4^{2-} (mM)	PO_4^{3-} (µM)	NH_4^+ (mM)	SiO_2 (µM)	K^+ (mM)	Na^+ (mM)	Sr^{2+} (µM)
164-991A-														
1H-1, 145–150	1.5	7.78	3.79	35.0	557	52.1	10.6	27.5	7	0.11	501	12.3	478	97
1H-2, 145–150	3.0	7.67	4.01	35.0	556	51.5	10.3	26.9	8	0.25	588	12.9	477	101
1H-3, 145–150	4.5	7.67	5.42	35.0	557	51.8	10.1	25.4	15	0.34	683	13.3	476	107
1H-4, 145–150	6.0	7.75	6.10	35.0	559	50.0	9.4	25.8	31	0.42	739	13.0	484	110
1H-5, 145–150	7.5	7.79	6.85	35.0	559	51.0	9.7	23.4	32	0.52	758	13.0	477	113
2H-1, 145–150	10.6	7.88	9.41	35.0	570	48.3	8.2	20.6	42	1.06	726	11.8	495	124
2H-2, 145–150	12.1	7.86	9.97	34.5	573	48.2	8.0	19.0	31	1.09	764	12.5	495	128
2H-3, 145–150	13.6	8.07	9.29	34.5	568	48.2	8.1	18.1	17	1.22	—	12.1	487	130
2H-4, 145–150	15.1	7.99	12.15	34.5	575	48.5	7.8	17.0	42	1.36	—	12.5	494	129
2H-5, 145–150	16.6	8.14	10.55	35.0	579	46.6	7.2	16.2	18	1.39	814	12.0	501	133

Notes: Alk = alkalinity, and Sal = salinity. Sodium was calculated based on charge balance with an average standard deviation of 0.67%. Measurements of other species are described in the "Inorganic Geochemistry" section of the "Explanatory Notes" chapter (this volume). — = measurement not made.

Only part of this table is produced here. The entire table appears on CD-ROM (back pocket).

Acoustic Velocity

P-wave velocity data for Hole 992A are sparse, but the available DSV and PWL data indicate that velocities vary most in the upper 12 m, averaging 1.53 km/s. DSV data obtained deeper than 22 mbsf are systematically offset from the *P*-wave velocity values but are consistent with relatively constant velocity with depth.

Undrained Shear Strength

Vane shear measurements yield a linear increase of 10 kPa/m in the uppermost 10 m of Hole 992A. Below 10 mbsf, the average increase in strength with depth is 1.2 kPa/m.

Natural Gamma Radiation

NGR data average 10 counts/s in Hole 992A. The greatest range of variability in NGR is in the uppermost 10 m of the hole, and the NGR anomaly of the greatest wavelength and amplitude occurs between 8.5 and 10 msbf.

Thermal Conductivity

Thermal conductivity data show a significant difference between the uppermost and lowermost parts of Hole 992A and the intervening section (12–35 mbsf). Conductivities in the upper 12 m and deeper than 40 mbsf average 1.15 and 1.07 W/(m·K), respectively, but values in the intervening section are a relatively constant 0.98 W/(m·K).

Physical Properties Units

At Site 992, two units can be delineated on the basis of physical properties measurements. Unit A extends from 0 to 11 mbsf and is distinguished from underlying Unit B by a pronounced change in nearly all the measured parameters, most notably thermal conductivity. Unit A correlates with lithostratigraphic Unit I, a deformed sequence containing clay conglomerates and soft-sediment deformation features. Unit B (11–50.75 mbsf) has constant or slowly varying physical properties as a function of depth. Physical properties Unit B correlates with lithostratigraphic Unit II, a homogeneous, undeformed sequence of diatom- and nannofossil-rich clay.

Hole 993A

Figure 42 shows the physical properties results obtained for Hole 993A.

Index Properties

Wet bulk density, porosity, and water content are remarkably homogeneous with depth. GRAPE and index properties determinations

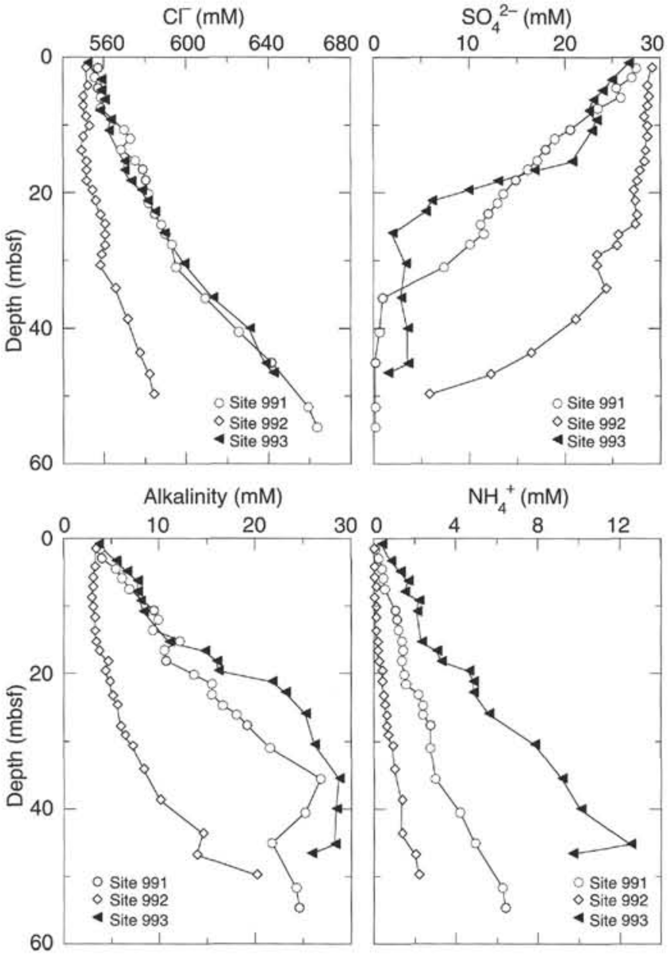

Figure 38. Interstitial-water concentration profiles for Sites 991, 992, and 993.

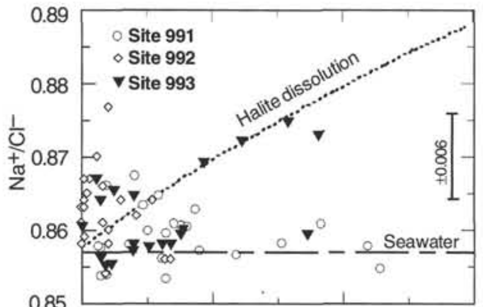

Figure 39. Graph showing Na^+/Cl^- vs. Cl^- concentration of interstitial water from Sites 991, 992, and 993 (after Brantley et al., 1984). The dashed horizontal line is the seawater Na^+/Cl^- ratio. Points falling on this line reflect seawater composition with varying chloride concentrations. The inclined dashed line is the mixing curve between seawater and water derived from the dissolution of halite; dissolution of halite should result in a Na^+/Cl^- ratio approaching 1. Note that the graph pictures one extremity of the total mixing regime. Measurement uncertainties are given by the error bar.

yield wet bulk densities that range from 1.4 to 1.8 g/cm³. Porosity decreases linearly as a function of depth, from 67% at the surface to 52% at the bottom of the hole. Water contents range from 33% to 42% (wet) and from 50% to 71% (dry) and decrease linearly as a function of depth.

Acoustic Velocity

P-wave velocity data are generally too poor to be used as the basis for analysis. The low-resolution DSV velocity determinations appear to be systematically higher than those obtained by the PWL but may indicate a change in *P*-wave velocity at 22 mbsf.

Undrained Shear Strength

The undrained shear strength of the uppermost 9 m of recovered core is constant at 70–80 kPa, but it increases gradually to 200 kPa by 25 mbsf. Vane shear measurements indicate, on average, continued strengthening of the formation with depth but show wide variability between 25 mbsf and the bottom of the hole.

Thermal Conductivity

The few thermal conductivity data obtained indicate a trend toward decreasing conductivity with depth, from >1.32 W/(m·K) at 0.75 mbsf to 1 W/(m·K) at 12 mbsf. Without deeper measurements, it is impossible to place this trend in context.

Physical Properties Units

Based on the relative homogeneity of physical properties with depth in Hole 993C, no units were distinguished. The only change in more than one physical property occurs at a depth of 1 mbsf, where wet bulk density drops from 1.8 to 1.6 g/cm³, porosity falls from 75% to 60%, and thermal conductivity decreases from 1.35 to 1.1 W/(m·K).

Discussion

The physical properties data can be used to infer the stress and sedimentation history of sediments overlying the Cape Fear Diapir. The data indicate that the shear strengths of sediments in the uppermost 2.5 m of Holes 991A, 992A, and 993A differ significantly (Fig. 43). At Site 991, shear strength is less than 10 kPa within the uppermost 2.5 m. In the same depth interval, shear strength reaches 20 kPa at Site 992. Site 993 has the highest shear strength at shallow depths, with vane shear and penetrometer measurements yielding undrained shear strengths of 75–90 kPa.

No evidence for pervasive cementation, diagenesis, or other processes that increase the strength of sediments was found in the recovered cores. The high strength measured in Core 164-993A-1H may, therefore, imply that the sediments in the shallowest part of Hole 993A have been exposed by the removal of the overlying sediments and are overconsolidated. Assuming that the stress history and bulk densities at Site 994 are similar to those at the Cape Fear Diapir, the strength vs. depth profile from Site 994 (see "Physical Properties" section, "Site 994" chapter, this volume) can be used to provide a quantitative estimate of the amount of overburden removed at Sites 991, 992, and 993. Little or no sediment was removed from Site 991. However, the comparison indicates that the strength of near-seafloor sediments in Holes 992A and 993A is consistent with the removal of ~4 m and 50–80 m of overburden, respectively. The inference that the removal of overburden caused overconsolidated sediments to be exposed at the seafloor at Site 993 is consistent with paleontological re-

Table 11. Index properties of sediment samples from Holes 991A, 992A, and 993A.

Core, section, interval (cm)	Depth (mbsf)	Water content (wet%)	Water content (dry%)	Density			Porosity (%)	Void ratio
				Bulk (g/cm^3)	Grain (g/cm^3)	Dry (g/cm^3)		
164-991A-								
1H-1, 135–137	1.35	52.97	112.62	1.49	2.78	0.70	77.10	3.06
1H-2, 138–140	2.88	47.20	89.38	1.56	2.77	0.82	71.78	2.41
1H-3, 138–140	4.38	48.27	93.33	1.54	2.63	0.80	72.53	2.40
1H-5, 132–134	7.32	40.12	66.99	1.63	2.68	0.97	63.67	1.75
2H-1, 72–74	9.82	39.22	64.52	1.72	2.78	1.04	65.66	1.75
2H-2, 130–132	11.90	39.48	65.23	1.72	2.71	1.04	66.15	1.72
2H-3, 120–122	13.30	42.97	75.34	1.65	2.75	0.94	69.33	2.02
2H-4, 124–126	14.84	40.43	67.87	1.66	2.63	0.99	65.53	1.74
2H-5, 116–118	16.26	41.13	69.85	1.65	2.63	0.97	66.17	1.79
3H-1, 116–118	19.76	40.96	69.37	1.69	2.71	1.00	67.56	1.83

Only part of this table is produced here. The entire table appears on CD-ROM (back pocket).

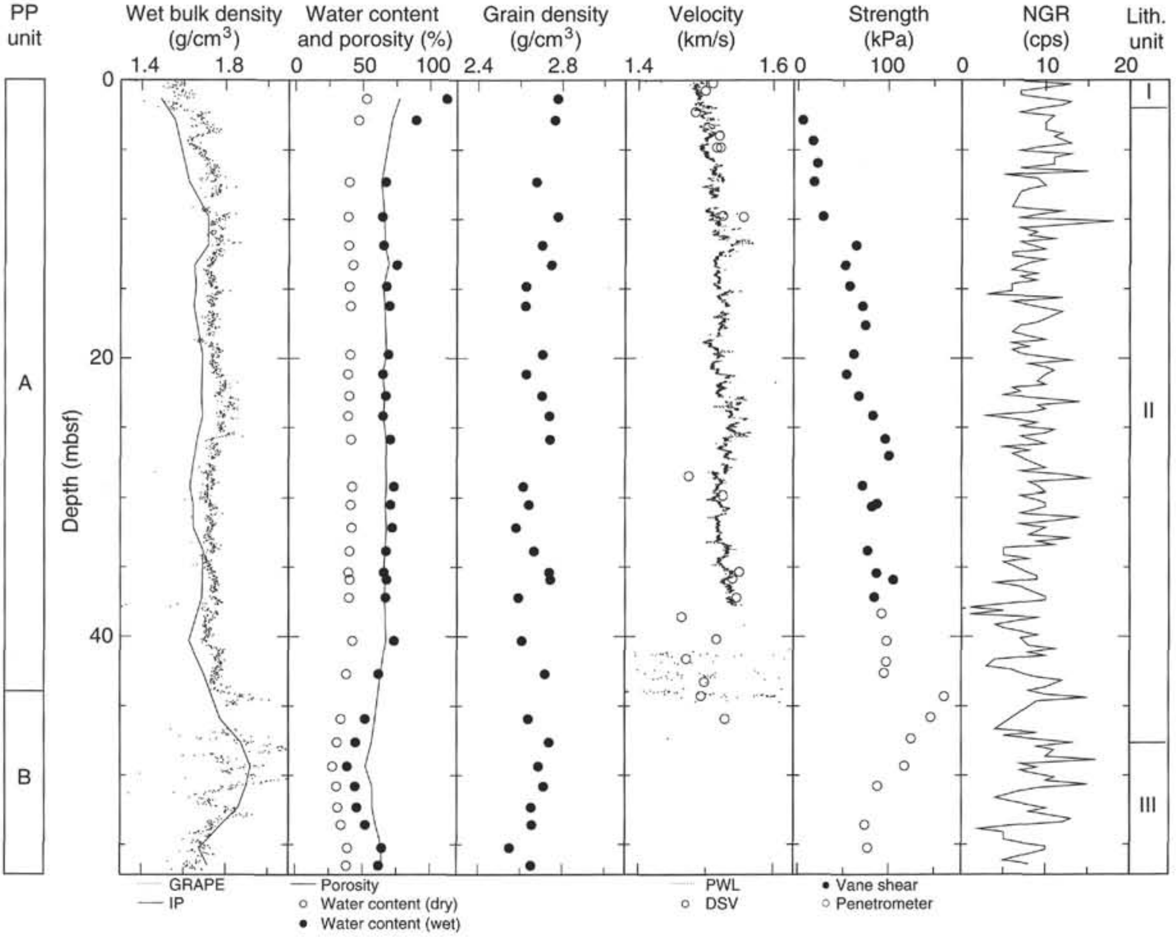

Figure 40. Physical properties measured in sediments recovered from Hole 991A. IP = index properties data, which are described in more detail in the "Physical Properties" section of the "Explanatory Notes" chapter (this volume). GRAPE = gamma-ray attenuation porosity evaluator data. Grain density has been measured using the dry method. PWL and DSV = velocity measurements made with the MST *P*-wave logger and the digital sound velocimeter, respectively. NGR = natural gamma radiation in average counts per second. Physical properties units are shown on the far left; lithostratigraphic units, on the far right.

sults indicating that the uppermost sediments are of late Miocene age (see "Biostratigraphy" section, this chapter).

SYNTHESIS AND SIGNIFICANCE

The major lithologies recovered from Sites 991, 992, and 993 are nannofossil-rich clay and nannofossil clay (10–60 wt% $CaCO_3$) with numerous intervals characterized by deformed beds and clay-clast conglomerates. The sediments are typical Neogene continental rise deposits and do not directly indicate the composition of the underlying diapir.

The sedimentary sequences recovered from Sites 991, 992, and 993 on the flank and crest of the Cape Fear Diapir have numerous stratigraphic gaps. Pre-Quaternary sediments occur between 0.5 and 30 mbsf at all three sites, indicating that the upper Quaternary section has been substantially truncated. Pervasive soft-sediment deformation was observed within the Pleistocene–Pliocene sequences from

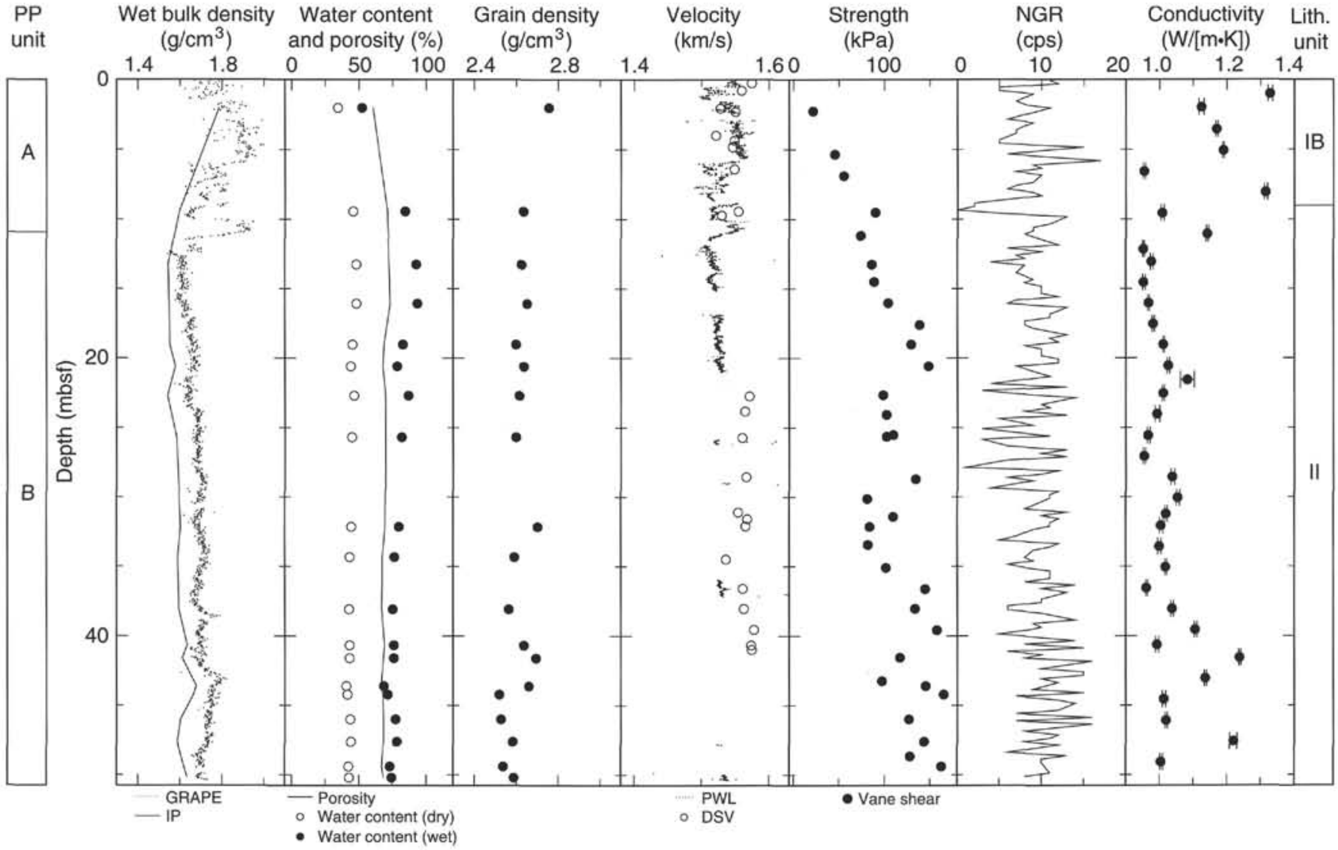

Figure 41. Physical properties measured in sediments recovered from Hole 992A. Vertical bars on conductivity data = analytical uncertainties. Physical properties units are shown on the left; lithostratigraphic units, on the right. The strength data were collected only with the vane shear apparatus. Abbreviations are the same as in Figure 40.

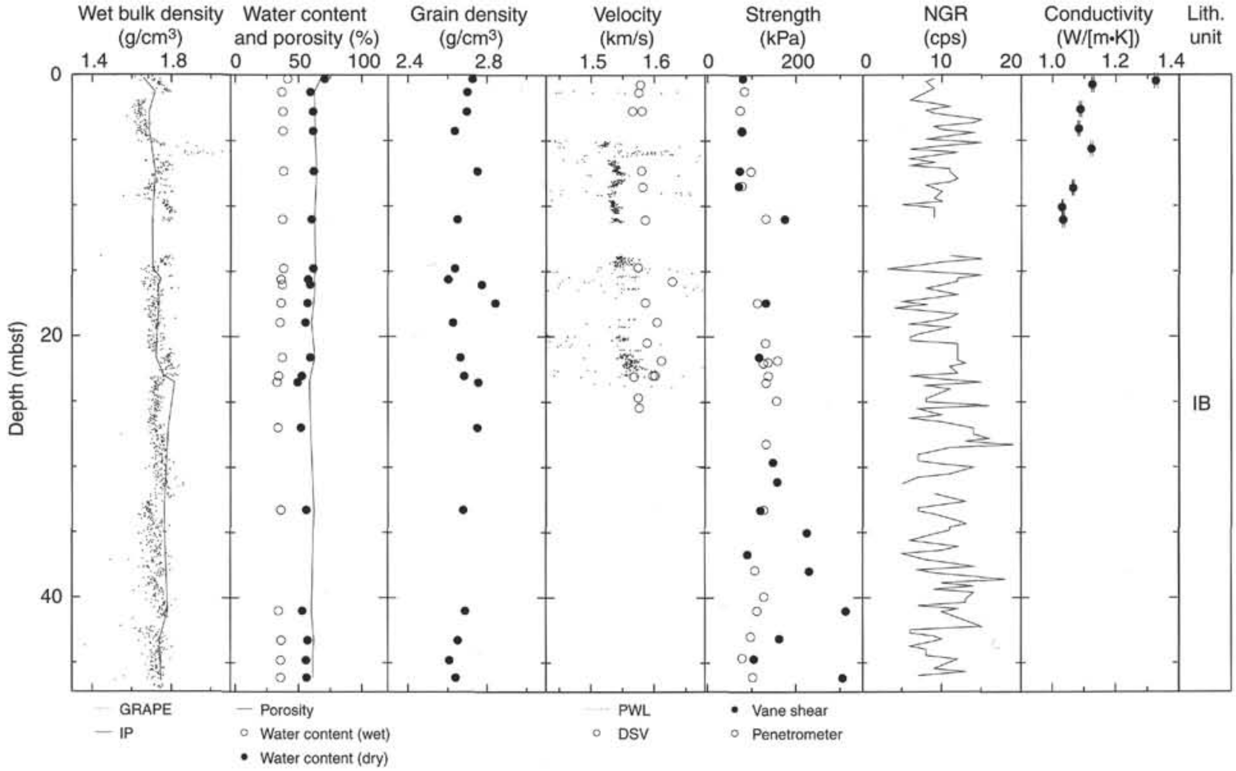

Figure 42. Physical properties measured in sediments recovered from Hole 993A. Vertical bars on conductivity data = analytical uncertainties. No units were distinguished on the basis of physical properties measurements. Lithostratigraphic units are shown on the right. Abbreviations are the same as in Figure 40.

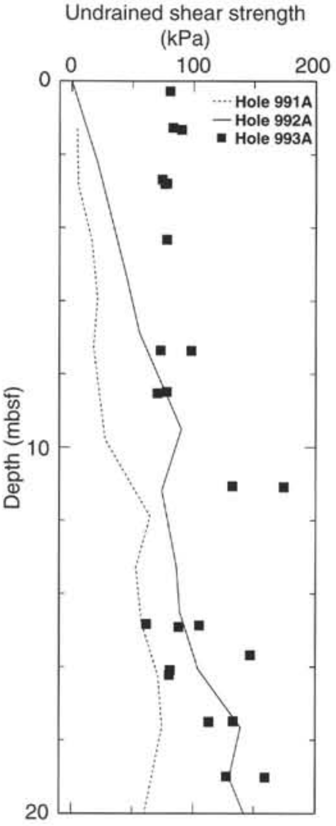

Figure 43. Undrained shear strength of sediments recovered from the upper 20 m in Holes 991A, 992A, and 993A. Both vane shear and pocket penetrometer results have been incorporated into this plot.

Sites 991 and 992, especially near the tops of both sections, suggesting that these unconformities resulted from vigorous mass-transport processes associated with sediment failures (e.g., slumping, sliding, and debris flows). The sediments near the surface tend to be overconsolidated for their current burial depths (see "Physical Properties" section, this chapter). The latest identified slide scar is either at or near the surface (2.05 m at Site 991, 0 m at Site 992, and 0.06 m at Site 993). The nannofossil stratigraphy indicates that other unconformities occur within some of the pre-Pleistocene sections. These deeper unconformities are associated with zones of soft-sediment deformation, suggesting that they also are the result of sediment failures.

Middle late Miocene material that is physically 19 m higher than the upper Miocene section at Site 991 occurs at Site 992. Apparently, the diapir has displaced the sediments on its crest upward at least 19 m with respect to the material on its upper flank.

The shortened or absent Holocene and upper Pleistocene sections in this region where Holocene and late Pleistocene sedimentation rates are known to exceed 20 cm/k.y. (Paull et al., 1996) indicates that the most recent deformation occurred within the late Quaternary and Holocene. The paucity of recent sediments around the diapir suggests that the diapir is still active. Pre-Quaternary deformation caused by diapiric uplift may also have occurred, but there is no evidence, such as biostratigraphic age reversals, to support this hypothesis. The question of whether the deformation is associated with disturbances generated by the emplacement of the diapir, or whether the sediment deformation is a result of the Cape Fear Slide, remains open.

Authigenic carbonate horizons, characterized by abundant fine-grained rhomb-shaped crystals, were encountered in intervals 164-991A-6H-1, 56–61 cm (~49 mbsf), and 164-993A-2X-3, 55–96 cm (~4 mbsf). X-ray analysis shows that some of the rhombs are dolomite. The origins of these horizons remain unclear; however, they are the only features observed that may indicate former fluid-flow conduits.

Methane/ethane ratios indicate that the gases sampled along this transect are predominately of a microbial origin. The increased interstitial-water chloride contents that are observed with depth at Sites 991, 992, and 993, coupled with the even greater increases at Site 996 (see "Site 996" chapter, this volume) suggest that these are salt-cored diapirs. However, the modest slope of these interstitial-water chloride gradients suggest that the salt core in these diapirs is still several kilometers below the seafloor. The complex geologic setting of these sites creates the possibility that several very different mechanisms control the lateral heterogeneity observed in the pore-water profiles. Fluid circulation associated with the diapir may drive circulation cells within the sediment, and the composition of the core material in the diapir may influence the interstitial-water chemistry. Gas hydrate at depth should cause ion exclusion (e.g., Kastner et al., 1990) so that upward diffusion of ions and/or advection of gas hydrate–associated fluids may further complicate these pore-water profiles. Truncation of interstitial-water profiles generated during slump events may still be equilibrating.

REFERENCES

Berner, R.A., 1984. Sedimentary pyrite formation: an update. *Geochim. Cosmochim. Acta,* 48:605–615.

Borowski, W.S., Paull, C.K., and Ussler, W., in press. Marine pore water sulfate profiles indicate in situ methane flux from underlying gas hydrate. *Geology.*

Brantley, S.L., Moller, N.E., Crerar, D.A., and Weare, J.H., 1984. Geochemistry of a modern evaporite: Bocana de Virrila, Peru. *J. Sediment. Petrol.,* 54:447–462.

Butler, R.F., and Banerjee, S.K., 1975. Theoretical single-domain grain-size range in magnetite and titanomagnetite. *J. Geophys. Res.,* 80:4049–4058.

Canfield, D.E., and Berner, R.A., 1987. Dissolution and pyritization of magnetite in anoxic marine sediments. *Geochim. Cosmochim. Acta,* 51:645–659.

Carpenter, G.B., 1981. Coincident sediment slump/clathrate complexes on the U.S. Atlantic continental slope. *Geo-Mar. Lett.,* 1:29–32.

Cashman, K.V., and Popenoe, P., 1985. Slumping and shallow faulting related to the presence of salt on the continental slope and rise off North Carolina. *Mar. Pet. Geol.,* 2:260–272.

Damuth, J.E., 1977. Late Quaternary sedimentation in the western equatorial Atlantic. *Geol. Soc. Am. Bull.,* 88:695–710.

Dillon, W.P., and Paull, C.K., 1983. Marine gas hydrates, II. Geophysical evidence. *In* Cox, J.L. (Ed.), *Natural Gas Hydrates: Properties, Occurrences, and Recovery:* Woburn, MA (Butterworth), 73–90.

Dillon, W.P., Popenoe, P., Grow, J.A., Klitgord, K.D., Swift, B.A., Paull, C.K., and Cashman, K.V., 1982. Growth faulting and salt diapirism: their relationship and control in the Carolina Trough, Eastern North America. *In* Watkins, J.S., and Drake, C.L. (Eds.), *Studies of Continental Margin Geology,* AAPG Mem., 34:21–46.

Dunlop, D.J., 1973. Superparamagnetic and single-domain threshold sizes in magnetite. *J. Geophys. Res.,* 78:1780–1793.

Egeberg, P.K., and Abdullah, M.I., 1990. The diagenetic factors controlling the dissolved organic carbon (DOC) in pore water from deep sea sediments (ODP Leg 113, Weddell Sea). *In* Barker, P.F., Kennett, J.P., et al., *Proc. ODP, Sci. Results,* 113: College Station, TX (Ocean Drilling Program), 169–177.

Emerson, S., and Hedges, J.I., 1988. Processes controlling the organic carbon content of open ocean sediments. *Paleoceanography,* 3:621–634.

Hall, S.A., and Sager, W.W., 1990. Paleomagnetic and rock magnetic properties of sediment samples from Ocean Drilling Program Leg 116, central Indian Ocean. *In* Cochran, J.R., Stow, D.A.V., et al., *Proc. ODP, Sci. Results,* 116: College Station, TX (Ocean Drilling Program), 337–344.

Heezen, B.C., Hollister, C.D., and Ruddiman, W.F., 1966. Shaping of the continental rise by deep geostrophic contour currents. *Science,* 152:502–508.

Hesse, R., and Harrison, W.E., 1981. Gas hydrates (clathrates) causing pore-water freshening and oxygen isotope fractionation in deep-water sedimentary sections of terrigenous continental margins. *Earth Planet. Sci. Lett.,* 55:453–462.

Hounslow, M.W., Bootes, P.A., and Whyman, G., 1990. Remanent magnetization of sediments undergoing deformation in the Barbados accretionary prism: ODP Leg 110. *In* Moore, J.C., Mascle, A., et al., *Proc. ODP, Sci. Results,* 110: College Station, TX (Ocean Drilling Program), 379–391.

Housen, B.A., and Musgrave, R.J., 1996. Rock-magnetic signature of gas hydrates in accretionary prism sediments. *Earth Planet. Sci. Lett.,* 139:509–519.

Hutchinson, D.R., Grow, J.A., Klitgord, K.D., and Swift, B.A., 1982. Deep structure and evolution of the Carolina Trough. *In* Watkins, J.S., and Drake, C.L. (Eds.), *Studies of Continental Margin Geology,* AAPG Mem., 34:129–152.

Jorgensen, N.O., 1987. Holocene methane-derived, dolomite-cemented sandstone pillars from the Kattegat, Denmark. *Mar. Geol.,* 88:71–81.

Karlin, R., 1990. Magnetite mineral diagenesis in suboxic sediments at Bettis Site W-N, NE Pacific Ocean. *J. Geophys. Res.,* 95:4421–4436.

Kastner, M., Elderfield, H., Martin, J.B., Suess, E., Kvenvolden, K.A., and Garrison, R.E., 1990. Diagenesis and interstitial-water chemistry at the Peruvian continental margin—major constituents and strontium isotopes. *In* Suess, E., von Huene, R., et al., *Proc. ODP, Sci. Results,* 112: College Station, TX (Ocean Drilling Program), 413–440.

Kvenvolden, K.A., Frank, T.J., and Golan-Bac, M., 1990. Hydrocarbon gases in Tertiary and Quaternary sediments offshore Peru—results and comparisons. *In* Suess, E., von Huene, R., et al., *Proc. ODP, Sci. Results,* 112: College Station, TX (Ocean Drilling Program), 505–515.

Kvenvolden, K.A., and Kastner, M., 1990. Gas hydrates of the Peruvian outer continental margin. *In* Suess, E., von Huene, R., et al., *Proc. ODP, Sci. Results,* 112: College Station, TX (Ocean Drilling Program), 517–526.

Langford, F.F., and Blanc-Valleron, M.M., 1990. Interpreting Rock-Eval pyrolysis data using graphs of pyrolizable hydrocarbons vs. total organic carbon. *AAPG Bull.,* 74:799–804.

Leslie, B.W., Lund, S.P., and Hammond, D.E., 1990. Rock magnetic evidence for the dissolution and authigenic growth of magnetic minerals within anoxic marine sediments of the California continental borderland. *J. Geophys. Res.,* 95:4437–4452.

Martens, C.S., and Berner, R.A., 1974. Methane production in the interstitial waters of sulfate-depleted marine sediments. *Science,* 185:1167–1169.

Millero, F.J., and Sohn, M.L., 1992. *Chemical Oceanography:* Boca Raton (CRC Press).

Musgrave, R.J., Collombat, H., and Didenko, A.N., 1995. Magnetic sulfide diagnesis, thermal overprinting, and paleomagnetism of accretionary wedge and convergent margin sediments from the Chile triple junction region. *In* Lewis, S.D., Behrmann, J.H., Musgrave, R.J., and Cande, S.C. (Eds.) *Proc. ODP, Sci. Results,* 141: College Station, TX (Ocean Drilling Program), 59–76.

Paull, C.K., Buelow, W.J., Ussler, W., III, and Borowski, W.S., 1996. Increased continental margin slumping frequency during sea-level lowstands above gas hydrate-bearing sediments. *Geology,* 24:143–146.

Paull, C.K., Schmuck, E.A., Chanton, J., Manheim, F.T., and Bralower, T.J., 1989. Carolina Trough diapirs: salt or shale? *Eos,* 70:370.

Popenoe, P., Schmuck, E.A., and Dillon, W.P., 1993. The Cape Fear landslide: slope failure associated with salt diapirism and gas hydrate decomposition. In *Submarine Landslides: Selective Studies in the U.S. Exclusive Economic Zone.* U.S. Geol. Surv. Bull., 2002:40–53.

Reeburgh, W.S., 1976. Methane consumption in Cariaco Trench waters and sediments. *Earth Planet. Sci. Lett.,* 28:337–344.

Roberts, A.P., and Turner, G.M., 1993. Diagenetic formation of ferrimagnetic iron sulphide minerals in rapidly deposited marine sediments, South Island, New Zealand. *Earth Planet. Sci. Lett.,* 115:257–273.

Schmuck, E.A., and Paull, C.K., 1993. Evidence for gas accumulation associated with diapirism and gas hydrates at the head of the Cape Fear slide. *Geo-Mar. Lett.,* 13:145–152.

Schoell, M., 1980. The hydrogen and carbon isotopic composition of methane from natural gases of various origins. *Geochim. Cosmochim. Acta,* 44:649–662.

Shipboard Scientific Party, 1992. Site 861. *In* Behrmann, J.H., Lewis, S.D., Musgrave, R.J., et al., *Proc. ODP, Init. Repts.,* 141: College Station, TX (Ocean Drilling Program), 239–299.

Speiss, F.N., and Tyce, R.C., 1973. *MPL Deep-Tow Instrument System:* La Jolla, CA (Scripps Inst. Oceanogr.), Ref. Ser. 73–4.

Stein, R., Brass, G., Graham, D., Pimmel, A., and the Shipboard Scientific Party, 1995. Hydrocarbon measurements at Arctic Gateways sites (ODP Leg 151). *In* Myhre, A.M., Thiede, J., Firth, J.V., et al., *Proc. ODP, Init. Repts.,* 151: College Station, TX (Ocean Drilling Program), 385–395.

Tauxe, L., Valet, J.-P., and Bloemendal, J., 1989. Magnetostratigraphy of Leg 108 advanced hydraulic piston cores. *In* Ruddiman, W., Sarnthein, M., et al., *Proc. ODP, Sci. Results,* 108: College Station, TX (Ocean Drilling Program), 429–439.

Thompson, R., and Oldfield, F., 1986. *Environmental Magnetism:* London (Allen and Unwin).

Ussler, W., III, and Paull, C.K., 1994. Effects of ion exclusion and isotopic fractionation on pore water geochemistry during gas hydrate formation and decomposition. *Geo-Mar. Lett.,* 15:37–44.

Ms 164IR-106

NOTE: Core-description forms ("barrel sheets") and core photographs can be found in Section 4, beginning on page 337. Forms containing smear-slide data can be found in Section 5, beginning on page 599. Forms containing thin-section data can be found in Section 6, beginning on page 623.